STUDY OF MISALIGNMENT EFFECTS IN THE CMS FORWARD HADRON CALORIMETER

A THESIS SUBMITTED TO
THE GRADUATE SCHOOL OF NATURAL AND APPLIED SCIENCES
OF
MIDDLE EAST TECHNICAL UNIVERSITY

BY

CEMALİ KILINÇ

IN PARTIAL FULFILLMENT OF THE REQUIREMENTS
FOR
THE DEGREE OF MASTER OF SCIENCE
IN
PHYSICS

JANUARY 2016

Approval of the thesis:

STUDY OF MISALIGNMENT EFFECTS IN THE CMS FORWARD HADRON CALORIMETER

submitted by **CEMALİ KILINÇ** in partial fulfillment of the requirements for the degree of **Master of Science in Physics Department, Middle East Technical University** by,

Prof. Dr. Gülbin Duran Ünver _____
Dean, Graduate School of **Natural and Applied Sciences**

Prof. Dr. Mehmet T. Zeyrek _____
Head of Department, **Physics**

Prof. Dr. Ali Murat Güler _____
Supervisor, **Physics Department, METU**

Examining Committee Members:

Prof. Dr. Ali Ulvi Yılmazer
Physics Engineering Department, Ankara University _____

Prof. Dr. Ali Murat Güler
Physics Department, METU _____

Prof. Dr. Ramazan Sever
Physics Department, METU _____

Prof. Dr. Altuğ Özpineci
Physics Department, METU _____

Asst. Prof. Dr. Kadir Öcalan
Civil Aviation Management Department, NEU _____

Date: _____

I hereby declare that all information in this document has been obtained and presented in accordance with academic rules and ethical conduct. I also declare that, as required by these rules and conduct, I have fully cited and referenced all material and results that are not original to this work.

Name, Last Name: CEMALİ KILINÇ

Signature :

ABSTRACT

STUDY OF MISALIGNMENT EFFECTS IN THE CMS FORWARD HADRON CALORIMETER

Kılınç, Cemali
M.S., Department of Physics
Supervisor : Prof. Dr. Ali Murat Güler

January 2016, 60 pages

The Compact Muon Selonoid (CMS) is a general purpose detector at the Large Hadron Collider (LHC). It is designed to investigate a wide range of physics, including the search for the Higgs boson and physics beyond the Standard Model. The CMS detector consists of various sub-detector systems, measuring energy, momentum, charge and trajectory of the particles produced by the proton-proton collision in the detector. The Forward Hadron Calorimeter (HF), a sub-system of Hadron Calorimeter (HCAL), identifies and measures the forward jets. It is designed as a rotational symmetric with respect to collision point. This leads total energy deposition to be symmetric in azimuthal direction (ϕ). Energy response of the readout channels are calibrated by using ϕ symmetry. However, misalignment of the HF breaks this symmetry. This study, simulation-based, focuses on the variations in the readouts geometry and total energy deposition due to misalignment of the HF. Moreover, the relation between geometry and total energy deposition is also studied.

Keywords: CERN, CMS, HF, ϕ symmetry, Misalignment

ÖZ

CMS İLERİ HADRON KALORİMETRESİNDE YANLIŞ HİZALAMA ETKİLERİNİN ÇALIŞILMASI

Kılınç, Cemali
Yüksek Lisans, Fizik Bölümü
Tez Yöneticisi : Prof. Dr. Ali Murat Güler

Ocak 2016 , 60 sayfa

Compact Muon Selonoid (CMS), Büyük Hadron Çarpıştırıcısında (BHÇ) yer alan genel amaçlı bir parçacık detektörüdür. Higgs bozonu ve Standart model ötesi fizik de dahil olmak üzere geniş çapta araştırma yapılmak için tasarlanmıştır. CMS detektörü, proton-proton çarpışmasından oluşan parçacıkların enerji, momentum, yük ve izlerini ölçen çeşitli alt detektörlerden oluşur. İleri Hadron Kalorimetresi (HF), Hadron Kalorimetresinin (HCAL) bir alt sistemi olup ileri jetlerin ölçümünde rol oynar. Çarpışma noktasına göre dönel simetrik olarak tasarlanmıştır. Bu özellik, HF e toplam enerji boşalımının ϕ simetrik olmasına neden olur. Bu simetri kullanılarak okuma kanalları kalibre edilir. Fakat, HF in yanlış hizalanması bu simetriyi bozar. Bu çalışma simulasyon temellidir, ve olası kayma durumunda okuma kanallarının geometrilerindeki değişimi ve toplam enerji boşalması değişimine odaklanır. Ayrıca, geometri ile toplam enerji boşalımı arasındaki bağıntı da incelenmiştir.

Anahtar Kelimeler: CERN, CMS, HF, ϕ simetrisi, Yanlış hizalanma

To My Family

ACKNOWLEDGMENTS

First and foremost, I would like to expess my deepest gratitude to my supervisor Prof. Dr. Ali Murat Güler for his guidance throughout the development of this study. By supporting my graduate studies at CERN, he has opened the academic path I will be following in the rest of my life. I would also like to thank to my thesis committee members Prof. Dr. Ramazan Sever, Prof. Dr. Altug Özpineci, Prof. Dr. Ali Ulvi Yılmazer and Asst. Prof. Dr. Kadir Öcalan for their kind attendance and suggestions.

Special thanks to Dr. Olga Kodolova for her support and encouragement during my studies at CERN. Her guidance has been such indispensable that this thesis would be impossible without her. I would also like to thank to CMS HCAL Calibration Group for letting me be a part of the group.

I have learnt much from the experience that Prof. Dr. Mithat Kaya and Dr. Özlem Kaya have conveyed to me. Their friendly approach also motivated me to undertake the hardwork that I have encountered.

Thanks to Eda Yıldırım who has not only been a great friend but also an academic mentor for me. When friendship is the issue, the names of Selda and Ali Motameni must be spelled. Thanks to them for furnishing my life with ease and joy against the most troublesome days. I would also like to thank to Sedef Beşkardeşler for the feelings blossomed inside me.

Great stress is endurable with great friends. In this regard, thanks to all my friends among which I can spell the names of İsmail Okan Atakişi, Candan Dözen, Gökçenur Yeşilyurt, Buğra Bilin, Metin Yalvaç, Mustafa Tek, Özgür Durmuş, Merve Demirtaş, Gökhan Alkaç, Altug Elpe and Muhteşem Akif Korkmaz.

I would like to note that this thesis is financially supported by the Turkish

Atomic Energy Agency with project no: CERN-A5.H6.F2-08.

Last but not least, I would like to thank to my mother and my brother for their love and support. I feel stronger for they always stand by me.

TABLE OF CONTENTS

LIST OF TABLES

TABLES

LIST OF FIGURES

FIGURES

CHAPTER 1

INTRODUCTION

CERN (Conseil Européen pour la Recherche Nucléaire), European Organization for Nuclear Research, is the largest research facility in the experimental particle physics field. It is an international organization and supported by many institutions all over the world. The Large Hadron collider (LHC) is the latest accelerator complex of CERN and it is the world's largest particle accelerator with its 27 km circumference.

The LHC has been designed to enlighten unsolved problems of particle physics such as the Higgs boson which explains the origin of mass according to the Standard Model and supersymmetric particles which can be an explanation of dark matter. On 4 July 2012, the Higgs boson has been found by two general purpose detectors of the LHC. Since the Standard Model does not predict the mass of the Higgs boson, its decay modes have not been known before 2012. In order to find the Higgs boson in intermediate mass region (114.5 GeV $c^{-2} < m_H < 2m_Z$) and high mass region ($2m_Z < m_H < 700$ GeV c^{-2}), good photon energy measurement, good electromagnetic energy resolution, efficient di-muon and di-electron mass resolution have been needed. For the Higgs in very high mass region (700 GeV $c^{-2} < m_H < 1$ TeV c^{-2}), good jet energy resolution and hadronic calorimeter that covers up to $|\eta| \leq 5$ have also been needed. Lowest mass supersymmetric particle can not be detected directly. Therefore, ${E_T}^{miss}$ (transverse missing energy) resolution of the detectors should be fine in order to detect such particle. For this purpose, energy of any detectable particle should be measured [20].

The Compact Muon Selonoid (CMS) is one of the general purpose particle detectors built at the LHC. The CMS is cylindrical shaped and each sub-detector has been designed as rotational symmetrical with respect to collision point. Due to this symmetry, energy deposited in each readout on a ring should be uniform. Therefore, they can be calibrated relatively. However, in the case of misalignment of any readout, relative calibration could not be possible and measurement becomes unreliable.

The Hadronic Forward Calorimeter is a sub-detector of the CMS and located at forward region. The HF is cylindrical shaped where center of the cylinder is on the beam axis and its skeleton is independent of the other sub-detectors. Therefore, shift of the skeleton does not affect other regions. Particles hit the HF does not pass through the other detectors,. Because of that reason, chance of the any readout parameter can not be detected by using data taken from other sub-detectors. This study focuses on the the effect of misalignment of the HF detector.

This thesis is composed of five chapters.

In Chapter 2, physics of the material particle interaction, which is the working principle of the calorimeters, is described.

In Chapter 3, the LHC accelerator and the CMS detector are presented. Information about all of the main sub-detectors is given. Moreover, their design purposes and their properties are discussed. In order for this study to be understood more clearly, geometrical and technical design details are also given.

The misalignment of the HF is discussed in Chapter 4. First, the calibration methods that are used for the HF are described. Then, effect of the HF shift on readout geometry is discussed. How the change of readout geometry affects the total energy deposition in readouts are shown.

The last part, Chapter 5 gives the summary of the study and a discussion about misalignment of the HF.

CHAPTER 2

PARTICLE INTERACTION WITH MATTER

Detectors used for measuring the energy of particles are called as calorimeters. Particle passes through the calorimeter, interacts with material and lose the energy. Lost energy is converted to signal, and energy of a particle can be measured. Mechanism of energy loss depends on the particle. In this chapter, particle interaction with matter and calorimeters will be presented.

2.1 Energy Loss Mechanism

Particles interact with matter via electromagnetic or strong interactions (weak interaction is not mentioned due to negligible cross-section). According to interaction type, calorimeters are divided into two groups; electromagnetic calorimeter and hadronic calorimeter. The HF is sensitive to both interaction and detects leptons and hadrons.

Electrons (positrons) and photons interact with matter through electromagnetic interaction. Electrons are charged particles and they can excite or ionize atoms of material. Moreover, they could emit radiation due to electromagnetic field. Emitted radiation is called Bemstrahlung. If the media is transparent and dielectric, high energetic charged particles cause media to emit Cherenkov radiation. High energetic photons lose their energies by creating electron-positron pairs.

Hadrons, in addition to electromagnetic, interact with material via strong interaction. As a consequence of this reaction, secondary particles could be produced. Detailed description of interactions playing a role in measurement of energies of

high energetic particles will be presented in the next section.

2.1.1 Ionization Energy Loss

Ionization is the primary energy loss process for heavy charged particles. Charged particle, passing through the media, gives some of its energy via interacting with atomic electron.The mean energy loss per unit length is calculated by the Bethe-Block equation,

$$-\langle\frac{dE}{dx}\rangle = Kz^2\frac{Z}{A}\frac{1}{\beta^2}[\frac{1}{2}ln\frac{2m_ec^2\beta^2\gamma^2T_{max}}{I^2} - \beta^2 - \frac{\delta(\beta\gamma)}{2}]\rho \qquad (2.1)$$

($K = 4\pi N_A r_e^2 m_e c^2$; z: charge of the particle; A: atomic mass of the material; T_{max}: maximum energy transfered to atomic electron in single collision; I: mean ionization potential of medium; δ: density correction; $r_e = e^2/4\pi\epsilon_0 m_e c^2 = 2.8fm$: classical electron radius)

Rate of energy loss for proton in various materials are shown in figure 2.1. Due to the β^{-2} term in the equation, rate of energy loss decreases until minimum ionization point ($\beta\gamma \approx 3GeV/c$). Beyond this point, curve increases logarithmically with $(\beta\gamma)^2$.

Working principle of gas detectors is ionization. When particle passes through the gas, energies of the ions are measured. If magnetic field is applied to the system, momentum can also be measured. Because, the energy loss depends on γ, rest mass of the particle could be calculated by measuring momentum and energy loss. This is used for particle identification (figure 2.2).

2.1.2 Bremstrahlung

Charged particle passing through the material interacts with nuclei electromagnetically and accelerates or decelerates due to electromagnetic force between them. The acceleration causes photon radiation, and this process is called as Bremstrahlung (breaking radiation in German) [2]. At high energies, electrons and positrons lose almost all their energies by this process.

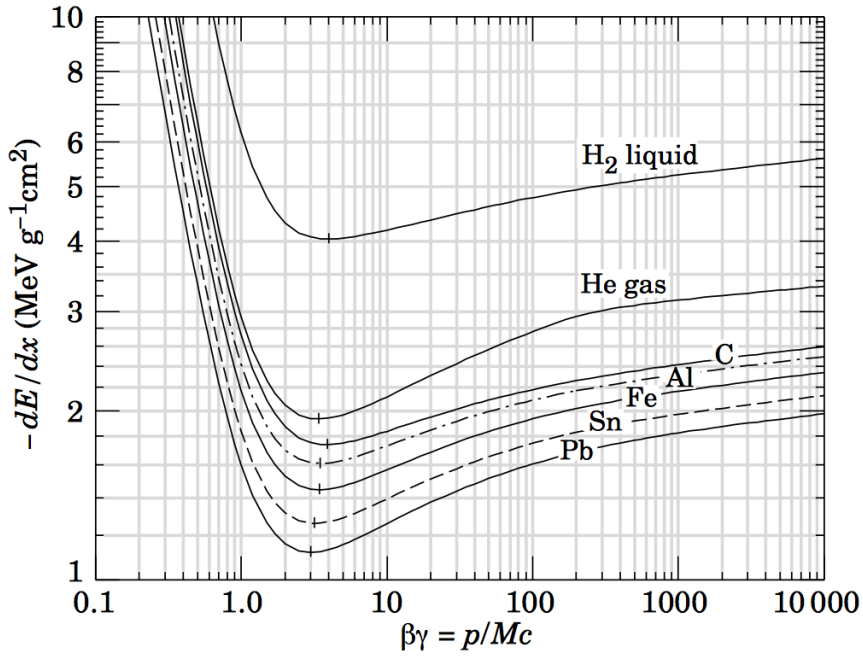

Figure 2.1: Ionization energy loss rates for protons in various materials [4].

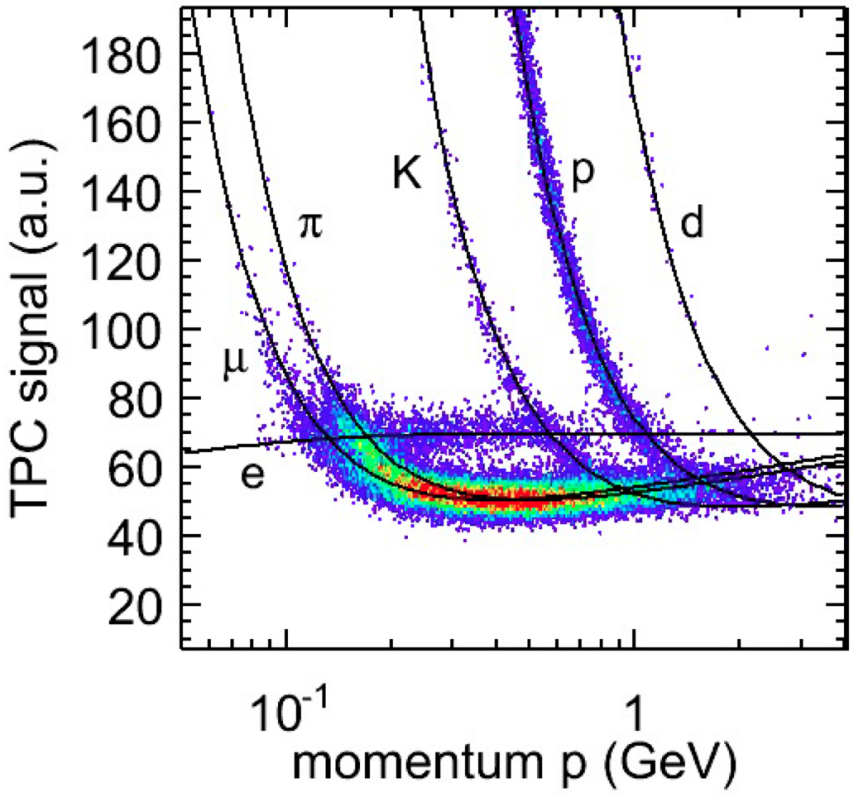

Figure 2.2: measurement of energy deposition in ALICE TPC.

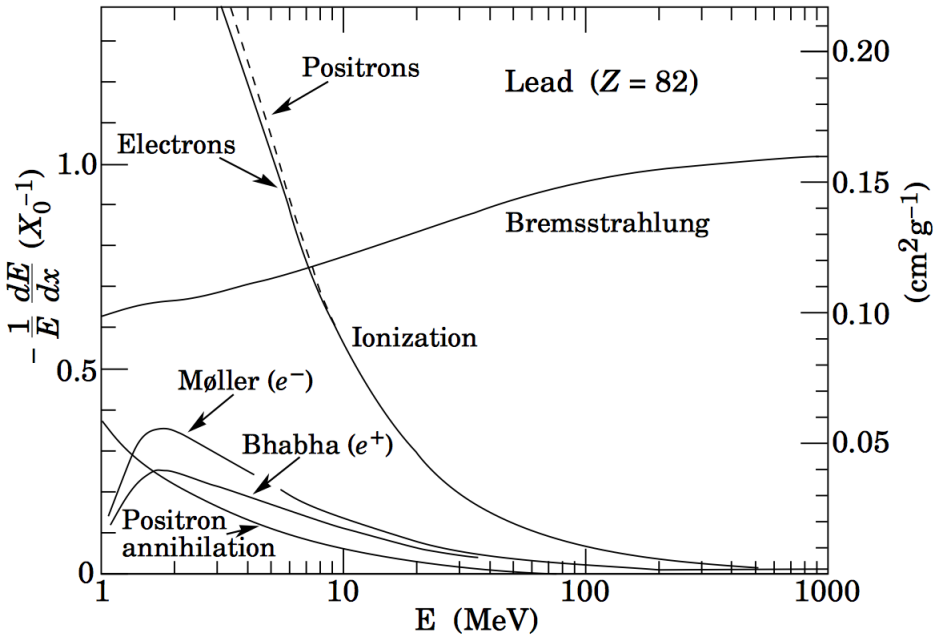

Figure 2.3: Processes contributing to energy loss of electron (positron) in lead [9].

The average rate of energy deposition for relativistic electrons is given by;

$$-\frac{dE}{dx} = \frac{E}{X_0} \tag{2.2}$$

and energy of particle after distance x in material;

$$E(x) = E_0 exp(-\frac{x}{X_0}) \tag{2.3}$$

X_0 is called as the radiation length that is average distance needed for interaction fulfilled and can be calculated as follows; $dp = n\sigma_{rad}dx$ is the probability of the interaction in dx interval, where n is atoms per cm^3 and σ_{rad} is the radiation cross-section. The distance makes probability 1 is X_0 ($1 = \int_0^{X_0} n\sigma_{rad}dx$) Therefore, X_0 is ;

$$X_0 = \frac{1}{n\sigma_{rad}} \tag{2.4}$$

2.1.3 Interaction of Photon with Matter

Three main processes are responsible for interaction of photon with matter: Photoelectric effect, Compton scattering and pair production [6]. Interaction of any

photon in beam with matter leads to decrease intensity of the beam. Therefore, instead of energy, intensity is used as quantity for explaining the behavior of interaction. Consequently, intensity of monochromatic beam of photon decreases by;

$$dI = -I\frac{dx}{\lambda} \tag{2.5}$$

where $\lambda = (n_a\sigma_\gamma)^{-1}$ is the mean interaction length. Hence, intensity function of distance is;

$$I(x) = I_0 exp(-\frac{x}{\sigma_0}) \tag{2.6}$$

Pair production is the dominant process at high energies. Cross-section for pair production is given by;

$$\sigma_{pair} = \frac{7}{9}\frac{1}{n_a X_0} \tag{2.7}$$

Therefore, Intensity function is;

$$I(x) = I_0 exp(-\frac{7x}{9X_0}) \tag{2.8}$$

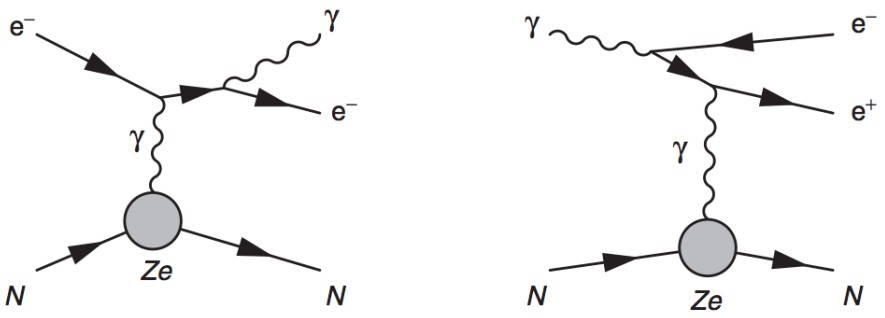

Figure 2.4: Feynman diagrams for Bremstrahlung and pair production.

2.1.4 Cherenkov Radiation

Cherenkov radiation is emitted by excited atoms, when a charged particle passes through a dielectric medium with reflective index n, at a velocity greater than $\frac{c}{n}$. Wavefront of emitted light is conical in shape, and it is emitted at angle θ to the particle trajectory [4].

$$\cos\theta = \frac{1}{\beta n(\lambda)} \tag{2.9}$$

where $\beta = \frac{v}{c}$ and $n(\lambda)$ is wavelength dependent reflective index.

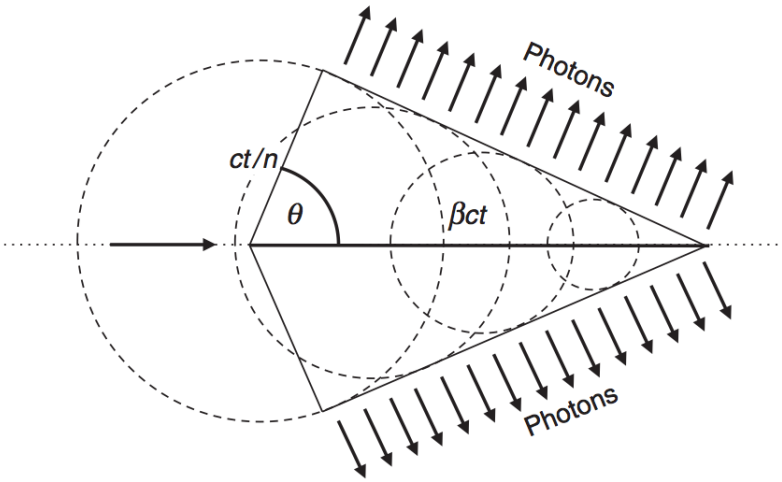

Figure 2.5: A conical wavefront makes θ angle with particle trajectory [8].

Cherenkov radiation is continuous spectrum, and the number of emitted photons is proportional to frequency. Therefore, dominant light is blue [2]. The number of emitted photon due to Ze charged particle in the interval $d\lambda$ in the unit length dx is given by;

$$\frac{d^2N}{d\lambda dx} = \frac{2\pi z^2\alpha}{\lambda^2}(1 - \frac{1}{\beta^2 n^2(\lambda)}) \tag{2.10}$$

Velocity of particle can be determined by either measuring θ angle of measuring the number of photons in a particular λ length [6].

2.1.5 Strong Interaction With Matter

Hadron interacts with atomic nuclei via strong nuclear force. This could be elastic or inelastic. At high energies, inelastic reaction are much more probable than elastic reaction. As a consequence of inelastic collision, new particles are produces in the final state.

The probability of a hadron interacting with matter in dx is given by; $n\sigma_{tot}dx$ where n is the number of atoms per unit volume. Mean distance passed through before any interaction (collision length) is;

$$l_c = \frac{1}{n\sigma_{tot}} \tag{2.11}$$

like collision length, absorption length is expressed as follows;

$$l_a = \frac{1}{n\sigma_{inel}} \tag{2.12}$$

At high energies, $l_a \approx l_c$, due to larger cross-section of inelastic reaction. Because of small cross-section of strong interaction, absorption length for 100 GeV hadron in iron is about 40 cm [4].

2.2 Electromagnetic Shower

As stated above, at high energies dominant interactions are Bremstrahlung for electron and pair production for photon. A high energetic electron entering the detector emits photon. Then, resulting photon produces e^-e^+ pairs and electron that emitted photon before, emits photon again. This process creates shower of electrons, positrons and photons. It continues until the critical energy [6].

A simplified explanation of the electromagnetic shower is given by the Heitler model [8]. According to the model, when any particle produces two new particles, produced particles share energy of mother particle equally. Production processes occur once in each radiation length. Schematic description of the model is shown in figure 2.6.

The particle with initial energy E_0 creates a shower containing 2^t particles after t radiation length. Each particle of the shower has average energy;

$$E(t) = \frac{E_0}{2^t} \tag{2.13}$$

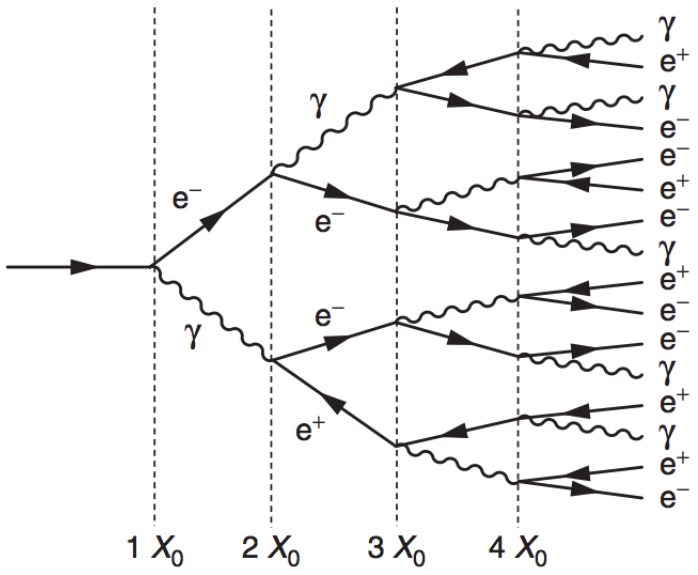

Figure 2.6: Electromagnetic shower development according to Heitler model [8].

The multiplication mechanism stops when $E(t) = E_c$ and radiation length is maximum at this point.

$$t_{max} = t(E_c) \tag{2.14}$$

And number of particles produced is;

$$N_{max} = exp[t_{max} ln2] = \frac{E_0}{E_c} \tag{2.15}$$

According to the model, number of particles increases exponentially until their energy reach critical energy. Then, energy deposition stops abruptly. However, in reality this is not the case. The curve has a long tail due to statistical fluctuations of the Bremstrahlung process. Therefore, energy deposition is simulated by using Monte-Carlo method, and it is explained by the gamma distribution,

$$\frac{dE}{dt} = E_0 b \frac{(bt)^{a-1} e^{-bt}}{\Gamma(a)} \tag{2.16}$$

where, a and b depend on type of the material. Maximum radiation length varies with respect to incident particle type (photon or electron). If incident particle

is photon, radiation length is ;

$$t_{max} = ln\frac{E}{E_c} + 0.5 \tag{2.17}$$

else ;

$$t_{max} = ln\frac{E}{E_c} - 0.5 \tag{2.18}$$

Electromagnetic calorimeters can separate electrons from photons by using this property.

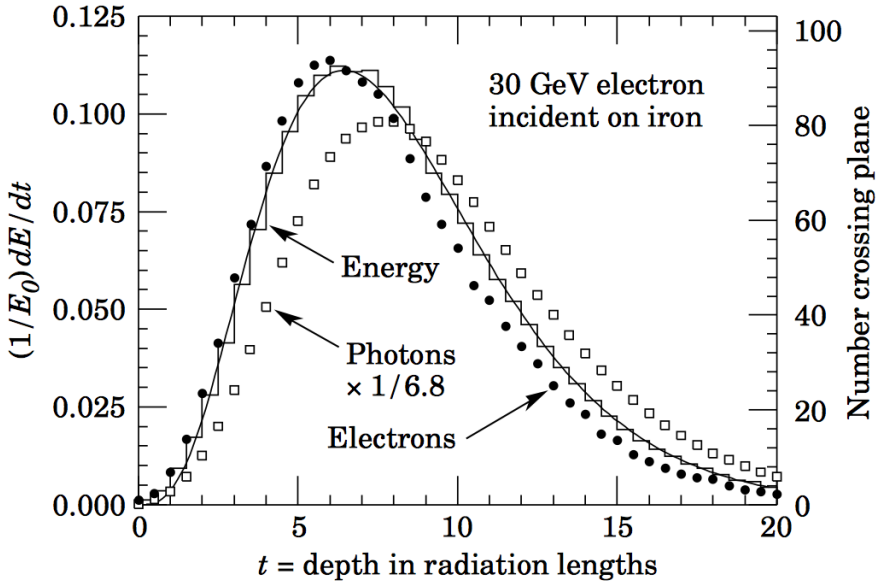

Figure 2.7: Monte-Carlo simulation of cascade in iron initiated by 30 GeV electron. Histogram indicate the energy deposition per X_0. Squares and circles represent the number of photons and electrons, respectively, passing through the planes at $X_0/2$ intervals [6].

2.3 Hadronic Shower

A hadronic shower is the result of inelastic nuclear collision. Even through it resembles electromagnetic shower, it is much more complex due to wide range of secondary hadrons [4]. The scale for longitudinal shower development is expressed by the nuclear absorption length. This leads hadronic calorimeters being thicker than electromagnetic calorimeters [2].

The HF is a Cherenkov calorimeter, and it is sensitive to electromagnetic showers. Therefore, electromagnetic component of the hadronic shower ($\pi^0 \rightarrow \gamma\gamma$) can be detected. Thus, hadronic energy resolution of the HF is worse than other subdetectors of the HCAL.

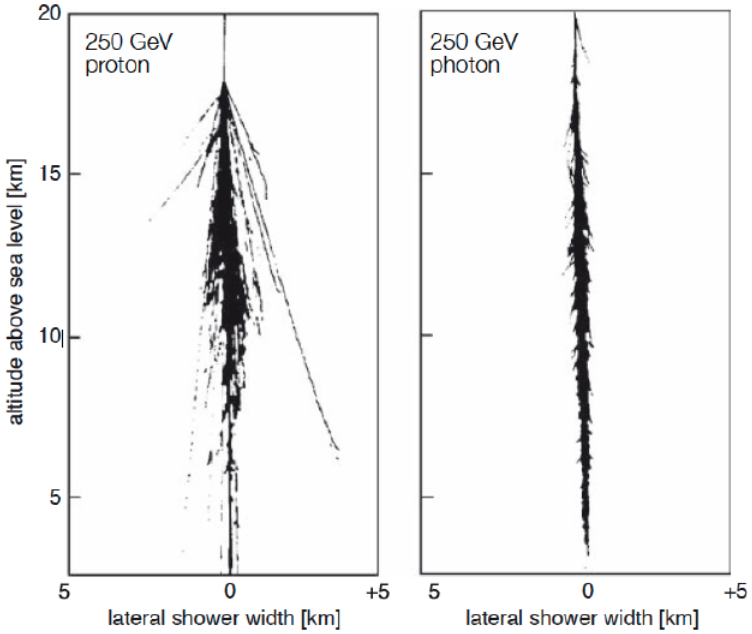

Figure 2.8: Electromagnetic and hadronic showers in air. While electromagnetic shower stops before sea level, hadronic shower continues. Moreover, transverse size of hadronic shower is larger than electromagnetic shower's [19].

2.4 Calorimeters

Calorimeters, apart from other detectors, detect both charged and neutral particles. Particles entering the calorimeter first interact with the medium and produces cascade of particles and lose significant amount of their energy. The medium that absorbs the particle energy is called as absorber. Deposited energy in the absorber creates signal in detector part of the calorimeter [4].

Some materials can function as both absorber and detector. Calorimeters consisting of this material, are called as homogeneous calorimeters. If absorber and detector are different materials, this type of calorimeter is called as Sampling Calorimeter. Homogeneous detectors have better energy resolution, and

they can detect every charged particle in the shower. However, low cost and containing high density absorber are advantages of sampling calorimeters.

The HF is a sampling calorimeter. Absorber and detector material in the HF are steel and quartz fiber, respectively. Particles that interact with steel create secondary charged particles. Signal is generated via Cherenkov radiation generated by secondary charged particles passing through quartz fibers [7]. Technical details of the HF will be discussed in Chapter 3.

CHAPTER 3

THE EXPERIMENT

The European Organization for Nuclear Research (CERN) is a multi-national research organization and includes the Large Hadron Collider (LHC). The LHC is designed to produce proton-proton collisions at very high energy. Particles produced as a result of the collisions are recorded by detectors operating at the LHC. The Compact Muon Selenoid (CMS) is a general-purpose particle detector built at the LHC. It is designed to search missing parts of the Standard Model and new physics models.

3.1 The Large Hadron Collider

The Large Hadron Collider (LHC) at CERN with its 27 km circumference is the largest circular accelerator ever built. It lays about 100m under surface across the French-Swiss national border near Geneva. In LHC tunnel, there are 1232 dipole magnets and 392 quadrupole magnets, each with magnetic field of 8.3 T, made of superconducting material niobium titanium (NbTi) and they are cooled below 2 K by using liquid helium [11]. Dipole magnets are used for bending the proton beams and quadrupole magnets are used for focusing the proton beams. The world's largest circular accelerator is designed to produce collisions of proton beams at center of mass energy ($\sqrt{s}$) of 14 TeV with instantaneous luminosity of $10^{34} cm^{-2} s^{-1}$. LHC began to collide proton beams at center of mass energy of 7 TeV in 2010. After three years in operation, in 2013 LHC shut down. During Long Shutdown 1(LS1), components of the accelerator and detectors are upgraded or repaired in order to operate at higher energies. After 2 years break

LHC started to operate at $\sqrt{s}$=13 TeV on 5 April 2015.

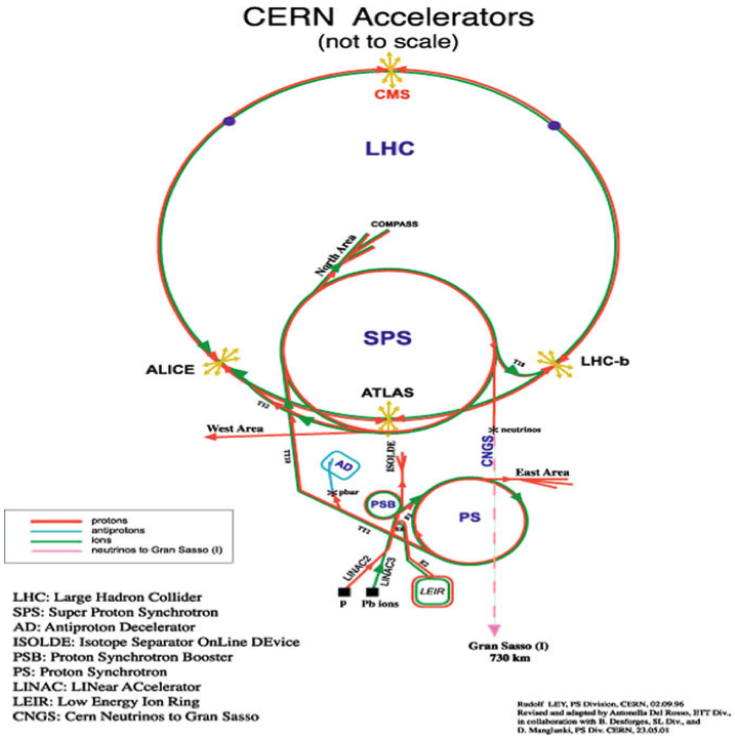

Figure 3.1: Schematic view of the CERN accelerator complex.

As it can be seen in Figure 3.1, before protons enter the LHC ring, they are accelerated in three different accelerators. Firstly they are boosted to 50 MeV by Linear Accelerator (LINAC), then they are injected to Proton Synchrotron (PS) so as to reach 1.4 GeV, and finally they are accelerated to 450 GeV by Super Proton Synchrotron (SPS). The LHC brings them to final energy with its 400 MHz radio frequency cavities. Opposing protons collide at four regions of LHC where different experiments are conducted. These experiments are CMS, ATLAS, ALICE and LHCb. CMS and ATLAS are general purpose experiments. ALICE and LHCb are specialized in physics of heavy ion collision and b physics respectively.

3.2 The CMS Detector

The Compact Muon Selonoid (CMS) detector is a general purpose particle detector built at LHC. The CMS is designed to search for Higgs boson and new physics beyond Standard Model such as supersymmetry or extra dimensions.

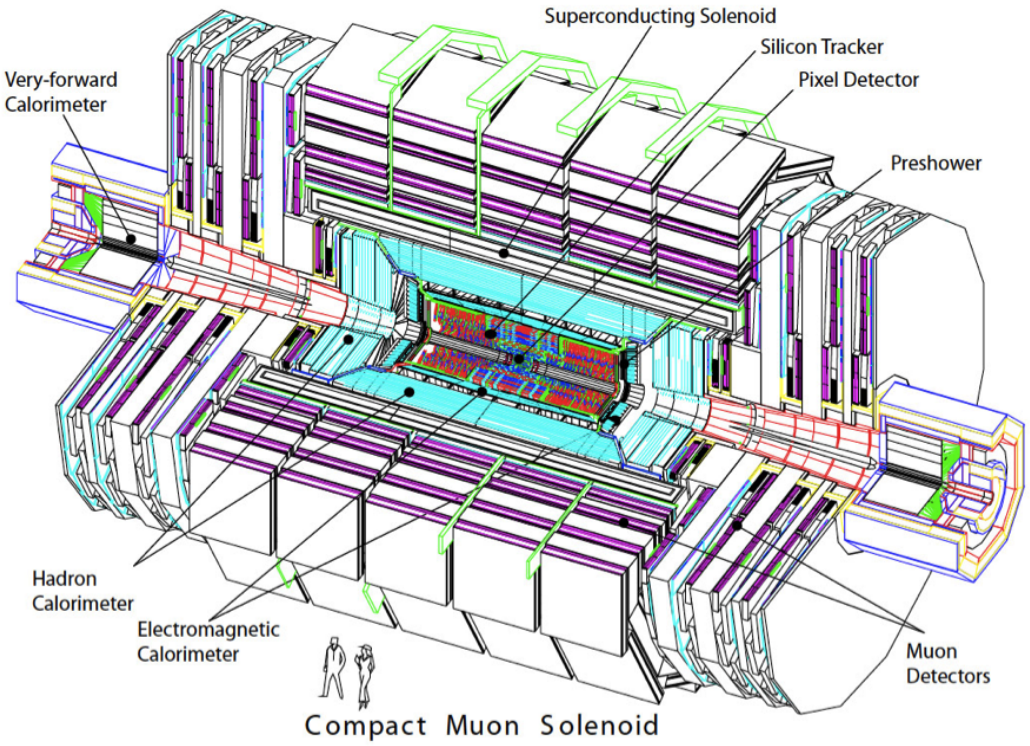

Figure 3.2: Sub-detectors of the CMS [10].

LHC is designed to produce collisions of proton beams at center of mass energy ($\sqrt{s}$) of 14 TeV with instantaneous luminosity of $10^{34} cm^{-2} s^{-1}$. The total proton-proton cross-section is expected to be approximately 100 mb [10]. Therefore, CMS will observe an event rate of 10^9 inelastic events/s. The huge rate must be reduced to about 100 events/s for storage. In order to achieve this, online event selection process (trigger) is used. The time between bunch crossings is 25 ns and about 1000 charged particles emerge from the collision point every 25 ns. The products of any interaction can be mixed up with those from other interactions in the same bunch crossing. If the response time of a detector is longer than 25 ns, this problem becomes more complicated. This phenomenon is called as pile-up. By using high-granularity detectors with good time resolution, the effect of pile-up can be diminished.

In order to reach the physics goals of LHC, CMS has to fulfill some requirements, these are can be summarized as follows:

- Good muon identification, good momentum resolution and good dimuon

mass resolution;

- Good particle momentum resolution. Efficient triggering and offline tagging of τ's and b-jets;

- Good electromagnetic energy resolution and π^0 rejection. Good dielectron and diphoton mass resolution;

- Wide geometric coverage, good E_T^{miss} and dijet-mass resolution.

CMS have been designed to meet these requirements. In order to measure momentum of muons, the magnetic field configuration is important. Moreover, large bending power is needed for precise measurement of the momentum of high-energetic charged particles. Because of that reason, superconducting technology is used for magnets.

The CMS detector has a cylindrical structure with a length of 21.6m and with a diameter of 14.6 m. As it can be seen in Figure 3.2, CMS is composed of several sub-detectors, these are, from the inner-most part to the outer-most part, the tracker, the electromagnetic calorimeter, the hadronic calorimeter and muon chambers. A 13-m long, 6-m inner diameter, 4 T superconducting selonoid creating a large bending power accommodates the inner tracker and the calorimeter inside.

The tracker measures charged particle trajectories and their vertices. It contains 3 layers of silicon pixel detectors and 10 layers of silicon microstrip detectors. The electromagnetic calorimeter (ECAL), with coverage up to $|\eta| < 3.0$, is used to measure the energy of electromagnetically interacting particles, especially photons and electrons. In front of the endcap region, there is a preshower system to reject π^0. HCAL, the next layer measures the energy of particles like ECAL, but it measures particles that interacts with strong force. The only particles pass beyond HCAL are muons and neutrinos. Existence of muons are detected by muon chamber detectors. Due to fact that muons are charged particles, momentum can be identified by measuring bending angle before muon system.

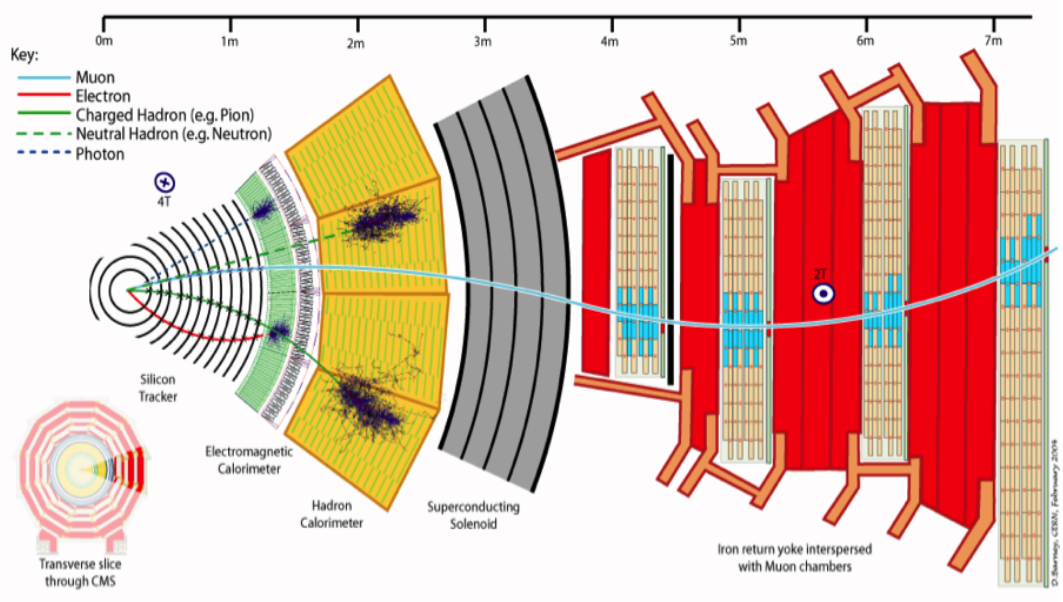

Figure 3.3: Transverse view of the CMS.

3.3 Coordinate Conventions

The origin of CMS is centered at the collision point. The x-axis is in direction from collision point to the center of LHC ring, the y-axis points vertically upward and the z-axis points along the beam direction. Generally, location of a particle is described by using the azimuthal angle, the radial distance and pseudorapidity. The azimuthal angle, ϕ is in the x-y (transverse) plane and measured from x-axis. The radial distance, r is defined in the transverse plane. The polar angle, θ is in y-z plane and measured from the z-direction.

The pseudorapidity is defined as η =-ln $\tan\frac{\theta}{2}$. The transverse momentum and transverse energy, denoted as P_t and E_t respectively, are computed from the x and y components. The transverse momentum and transverse energy are calculated as P_t=P$\sin\theta$ and E_t=E$\sin\theta$ respectively. Missing transverse energy, denoted by E_T^{miss}, is the undetected energy and calculated indirectly by using conservation of energy.

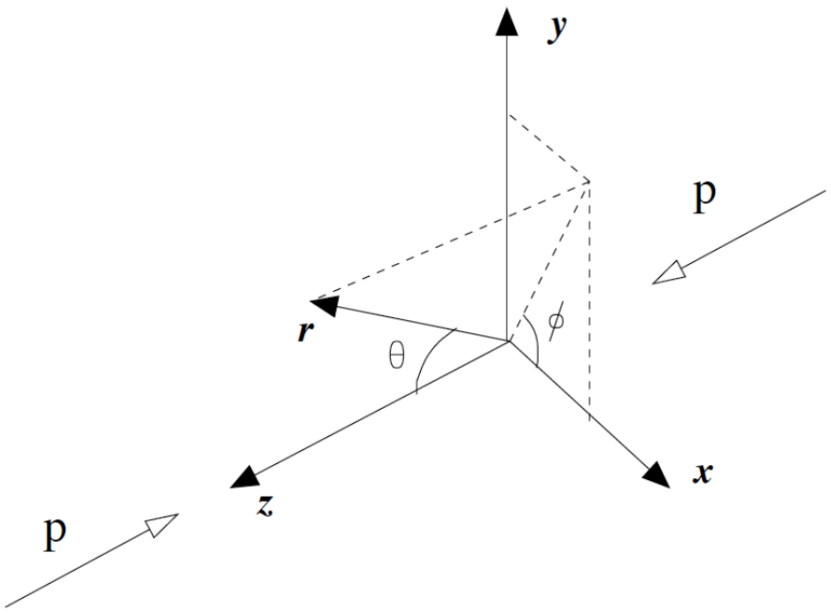

Figure 3.4: Coordinate system of the CMS.

3.4 Tracking Detectors

The tracker, with a radius of 1.25m and a length of 5.5m, is situated around the interaction vertex. It is designed to measure the trajectories of charged particles produced at LHC. Owing to inner radii of the CMS tracker is 4.4 cm, it also provides a precise reconstruction of secondary vertices. At LHC design luminosity, there will be about 1000 particles traversing the tracking volume in each bunch crossing. Hence high granular structure and fast detector response is needed in order to identify the trajectories correctly. Because of the intense particle flux , the detector must be radiation resistant. These requirements lead to the tracker based on silicon technology.

The CMS tracker is composed of a pixel detector and a silicon strip tracker. The pixel detector contains three barrel layers at radii 4.4 cm, 7.3 cm and 10.2 cm, and two endcap disks at a distance of z=$\pm$34.5, $\pm$46.5 cm from the interaction vertex. Pixels, with a size of 100x150 μm^2, form silicon sensor modules. The pixel detector consists of 1440 modules with a total 66 million readout channels. The silicon strip tracker, with 11.4 million strips, surrounds the pixel detector.

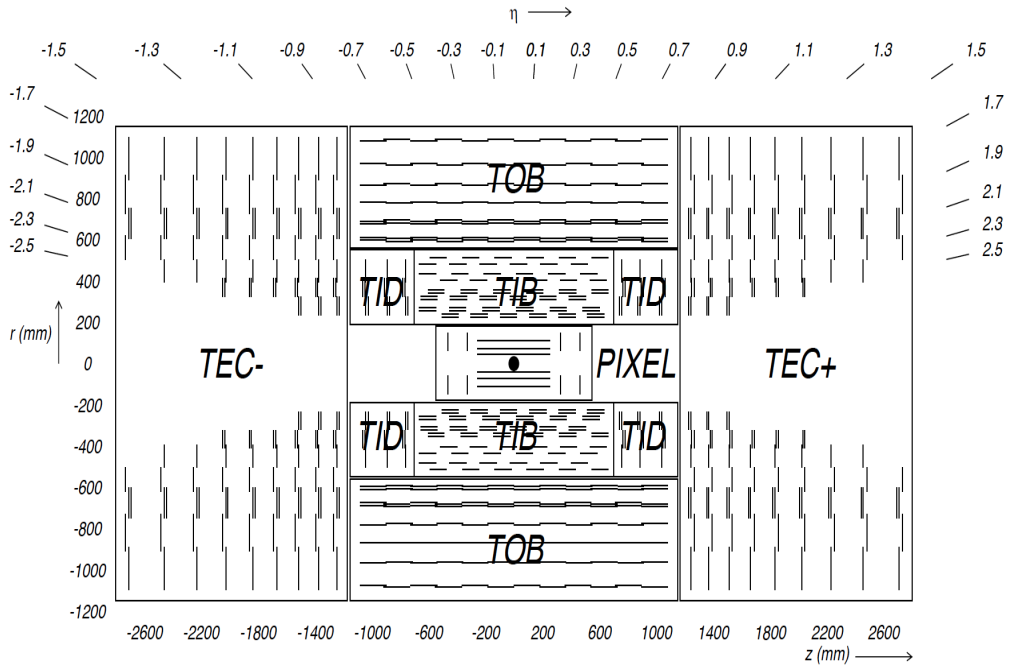

Figure 3.5: r-z view of CMS tracking detectors [10]. Single line represents a detector module. Double lines point out back-to-back modules.

It covers in pseudorapidity up to $|\eta| < 2.5$. As it can be seen in Figure 3.5, the silicon strip tracker is composed of four subsystems which are Tracker Inner Barrel (TIB), Tracker Outer Barrel (TOB), Tracker Inner Disk (TID) and Tracker Endcap (TEC). While the TIB, the TID and the first four rings of the TEC are composed of single-sided modules, the TOB and the last three rings of TEC consist of double-sided modules which are made from two single-sided modules attached back-to-back at an angle of 100 mrad.

3.5 The Electromagnetic Calorimeter

The Electromagnetic calorimeter (ECAL) is designed to measure energy of electrons and photons. As a scintillating material, lead tungstate crystal ($PbW0_4$) has been chosen. Lead tungstate is fast and radiation resistant. Moreover it has short radiation length (X_0=0.89 cm) which makes the calorimeter more compact. The crystal produces photons when particle passes through it. The

produced photons are converted to electronic signals by photodetectors.

The ECAL is composed of two parts which are central barrel part and endcaps. The central barrel consists of 61,200 crystals and the endcaps are composed of 7324 crystals. The front face cross-section of the crystals in the barrel and in the endcaps are 22x22 mm^2 and 28.6x28.6 mm^2, respectively. This explains fine granular structure and good spatial resolution of the calorimeter.

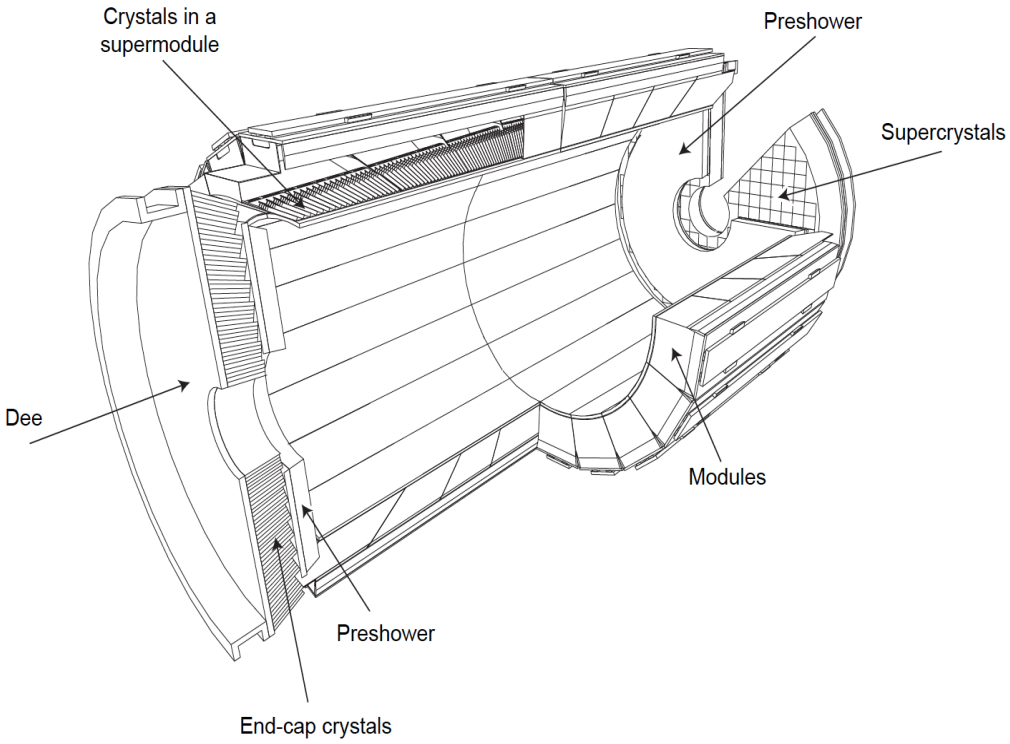

Figure 3.6: Layout of the CMS Electromagnetic Calorimeter [11].

The barrel (EB) covers the pseudorapidity up to 1.479 and its front face is at 1.29m from the beam axis. EB is divided into 360 cells in azimuth and 85 cells in pseudorapidity. The radiation length of the barrel crystal is $25.8X_0$, which corresponds to 23 cm. The signals generated by crystals are read out by using avalanche photodiode(APD).

The endcaps (EE), covering the pseudorapidity range $1.479<|\eta|<3.0$, are located on either side of the interaction point and 314 cm away from vertex. The radiation length of the endcap crystal is $24.7X_0$, that corresponds to 22 cm. Owing to the presence of the preshower detectors in front of the endcaps, the radia-

tion length shorter than for the barrel. The light generated by endcap crystal is read out by using more radiation resistant detector than APD,Vacuum PhotoTriode(VPT).

The preshower detector, covering the pseudorapidity range $1.65<|\eta|<2.5$, sits in front of the endcaps. In that region, the angle between two photon coming from neutral pion is small enough to mimic high-energy photon, the preshower detector is designed to prevent such false signals. The detector composed of two planes of lead and silicon detectors. It has finer granularity than the endcaps', and can separate two photons produced by natural pion decay.

The Energy resolution of the ECAL depends on the energy and is parametrized as:

$$(\frac{\sigma_E}{E})^2 = (\frac{S}{\sqrt{E}})^2 + (\frac{N}{E})^2 + C^2 \tag{3.1}$$

where S is the stochastic term, N is the noise and C is the constant.

3.6 Hadronic Calorimeter

The Hadronic Calorimeter (HCAL) is specialized to measure the particles composed of quarks and gluons such as protons, neutrons, pions and kaons. In addition to energy measurement, the HCAL can measure position and arrival time of the hadrons. The HCAL is built with no dead areas in ϕ, in order to measure missing transverse energy reliably. Hence, non-interacting particles such as neutrinos can be indirectly measured. The Calorimeter is sectioned into four distinct sub-detectors: the barrel (HB) covering the pseudorapidity range $|\eta|<1.3$, the hadronic outer (HO) having the same pseudorapidity coverage with the HB, the endcap (HE) at $1.3<|\eta|<3$ and the forward calorimeter (HF) covering up to $|\eta|<5.2$.

The barrel(HB) and the endcap(HE) consist of brass layers and plastic scintillators between them. The HO is between the ECAL and the solenoid and the amount of space for the absorber is limited. Therefore, brass has been used as

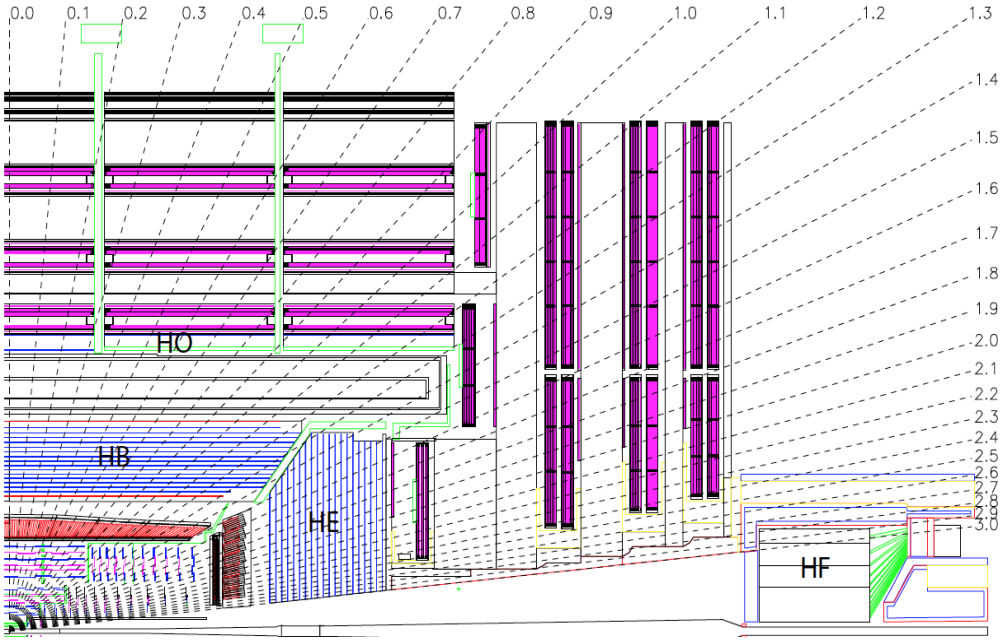

Figure 3.7: Longitudional view of the HCAL [11].

absorber material for its short interaction length. The plastic scintillator emits blue-violet light when particle passes through it. The blue-violet light is shifted to green light by wavelength shifting fibers in order to not to harm the detector. Then, the green light is read out by Hybrid Photo Detector (HPD). The scintillator is divided into 16 segments which forms the tower structure of the HCAL(see Figure 3.7).

The Hadron outer(HO) is located between the selonoid and muon system, to improve energy measurement of the HB. It uses the selonoid as absorbing material in addition to the HB. It is necessary to measure missing transverse energy accurately.

The forward calorimeter (HF) is made from steel absorbers and quartz fibers and it detects the Cherenkov radiation emitted by charged shower particles to measure the energy. The HF is discussed in more detail below.

3.6.1 Hadron Forward Calorimeter

Hadron Forward (HF) calorimeter is subdetector of Hadron Calorimeter(HCAL) and located outside of the selonoid. Two main objectives of HF are to improve the measurement of the missing transverse energy and to enable identification of very forward jets. HF is a cylindrical steel structure with outer radius 130 cm and has cylindrical hole for beam pipe with radius 12.5 cm from the center of the beam axis. The front faces of HF are located at 12.2 m away from the collision point. The Forward Calorimeter covers pseudorapidity range of $2.853<|\eta|<5.191$, in order to detect particles at relatively small angles from the beamline.

The absorber in HF is 1.65m long in the direction of the beam line. It is composed of 5 mm thick steel plates that contain holes running parallel to the beam axis and spaced out 5 mm from center to center [13]. The quartz fibers are inserted into holes in the composed steel absorber. The quartz fibers inside the holes are chosen as the active medium and are connected to PMTs in Readout boxes. The signal is carried by these quartz fibers. The source of the signal is Cherenkov radiation from charged shower particles above the Cherenkov threshold($E\geq 190$ keV for electrons) [11].

Although the HF is a subdetector of HCAL, it acts as both electromagnetic and hadronic calorimeter. This is achieved by dividing the detector into two longitudinal segments. Half of the fibers begin at the depth of 22 cm from the front face, while the other half run over the full depth of the absorber. The Long fibers and short fibers are readout by different PMTs. Because electromagnetically interacting particles depose their energies in the first 22 cm, the signals generated by electromagnetic showers and hadronic showers can be distinguished by this arrangement.

Each of HF calorimeters(HF+ and HF-) is divided into 18 wedges of 20° along the azimuthal direction. Each wedge is composed of 24 towers. There are 13 towers along η direction, and the ϕ segmentation of the towers is 10°, except the two high-eta towers, their segmentation 20°. There are totally 432 towers and

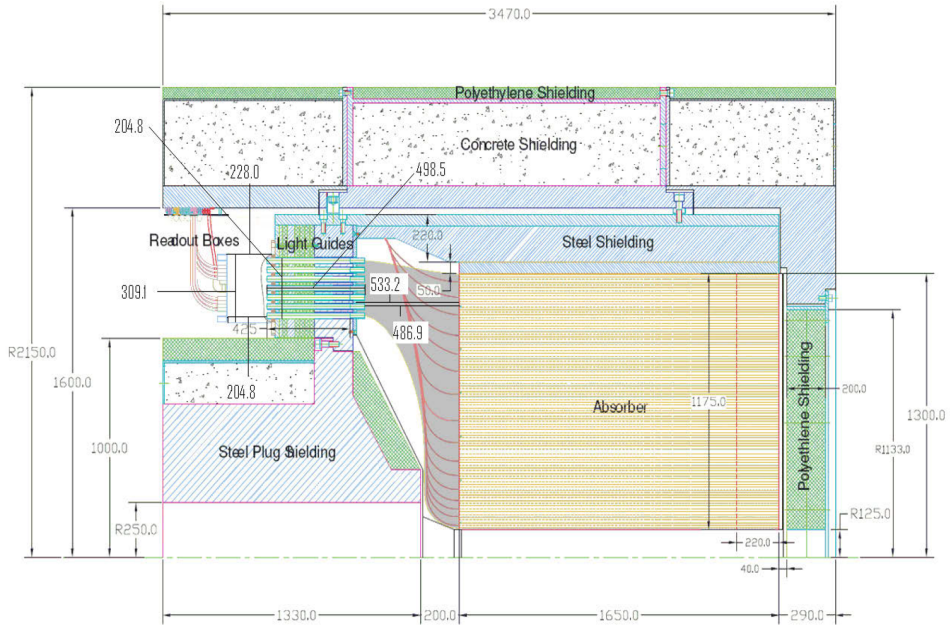

Figure 3.8: Longitudinal view of the HF [13].

Table3.1: η values of the towers and tower sizes.

$i\eta$	Low η	High η	Size in η	Size in ϕ
29	2.853	2.964	0.111	10°
30	2.964	3.139	0.175	10°
31	3.139	3.314	0.175	10°
32	3.314	3.489	0.175	10°
33	3.489	3.664	0.175	10°
34	3.664	3.839	0.175	10°
35	3.839	4.013	0.174	10°
36	4.013	4.191	0.178	10°
37	4.191	4.363	0.172	10°
38	4.363	4.538	0.175	10°
39	4.538	4.716	0.178	10°
40	4.716	4.889	0.173	20°
41	4.889	5.191	0.302	20°

864 channels in one HF module.

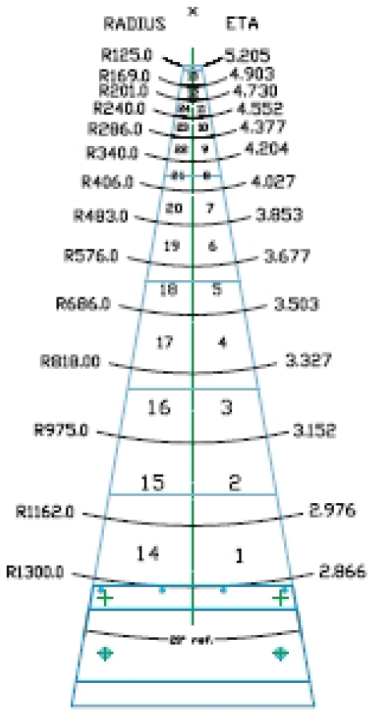

Figure 3.9: HF wedge [13].

3.7 Muon System

The Muon System, covering the region $|\eta|<2.4$, is located at the outer-most layer of the CMS [10]. Because, muons can not be stopped by any sub-detector of the CMS, energy can not be measured directly. The muon system has been designed for muon identification, momentum measurement and triggering. The muon system is based on gaseous detectors, and three types of gaseous detectors are used. Due to cylindrical structure of the CMS, the muon system is divided into barrel section and endcap section.

In the barrel region that covers pseudorapidity $|\eta|<1.2$, Drift Tube (DT) is used [10]. The drift tube is 4 cm wide and contains a positive charged wire inside. When charged particle passes through the tube, atoms inside the tube ionize and electrons hit the stretched wire in the middle. Therefore, the distance between

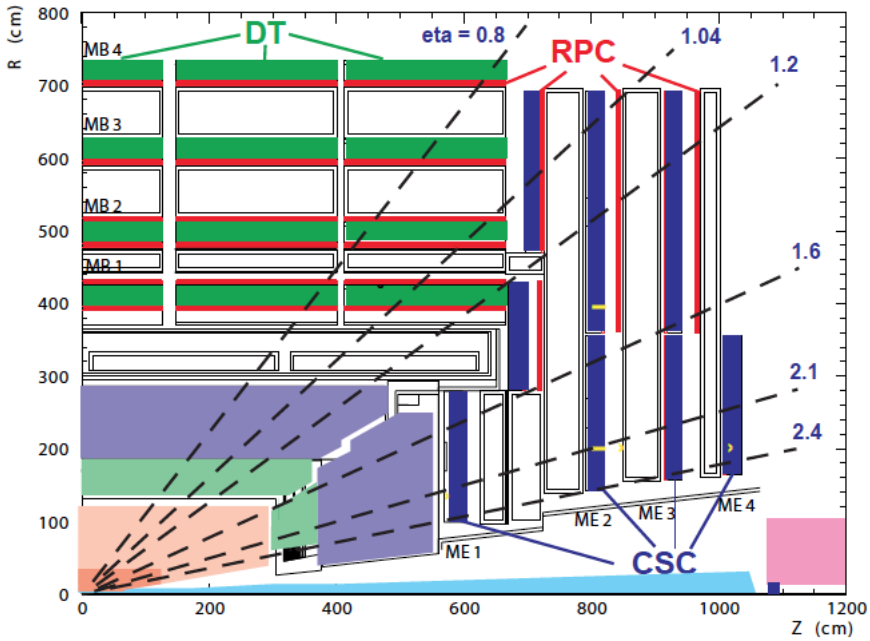

Figure 3.10: r-z view of the Muon system [11].

muon and the wire can be calculated. The drift tubes form DT chamber that is 2x2.5 m in size and is composed of 12 layers of DT cells (three groups of four). The DT chambers are arranged into 4 stations that are interleaved with the flux return plates in each ϕ sector. This arrangement provides 3-D position measurement, as well as, the muon time measurement.

In the endcap regions, covering the pseudorapidity range of $0.9<|\eta|<2.4$, the muon rates and the background levels are high. Cathode strip chamber (CSC) is used due to its fast response time and its fine granularity. The CSC is multiwire proportional chamber which consist of arrays of anode wires crossed with strips in a gas volume. Each endcap is composed of 4 CSC stations. They measure 2-D position of a muon and beam-crossing time of a muon [10].

The Resistive Plate Chambers (RPC) used as trigger system in both the barrel and endcap sections. The RPC consists of two high resistive parallel plates, readout strips on top of the plate and gas between plates. The RPC can measure the momentum of the muons with a time resolution of 1ns. Therefore, it immediately decides to take data or not and trigger whole system behind.

3.8 Trigger

The time between bunch crossing is 25 ns at LHC and it corresponds to frequency of 40 MHz. At design luminosity this frequency leads to 10^9 interactions per second. Since it is not possible to write the data at bunch crossing rate and the most of the data forms the background, the trigger system is used to reduce 40 MHz event rate to 100 Hz in order to store an event permanently. The purpose of the trigger system is to select interesting events such as Standard model Higgs, any unknown particle, top events, WW, ZZ, Wγ and many others. Background events come from the collisions that include no new information. Moreover, The trigger selects events used for calibration and testing. The trigger system mainly composed of hardware based Level-1 Trigger (L1T) and software based High Level Trigger (HLT).

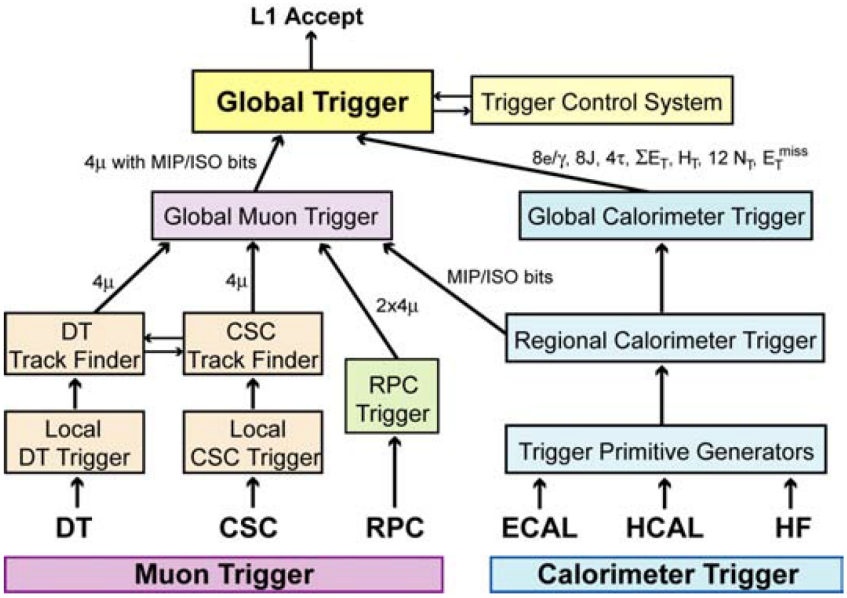

Figure 3.11: Architecture of the L1 trigger [10].

The Level-1 Trigger is made of programmable electronic chips and logic units, since the decision to reject or accept an event is needed to be taken in a short period of time. The muon trigger and the calorimeter trigger are linked via the global trigger. The sub-triggers select interesting physics objects (candidate electrons, photons, muons or jets) and sort them according to their rank based on transverse energy and momentum. The highest rank objects are sent to the

global trigger where the decision is taken by applying the selection criteria based on physics or technical requirements. The L1 trigger reduces the event rate to 100 kHz.

The events selected by the L1 trigger are sent to High Level Trigger for further filtering. The processors in the computer farm parallelly execute HLT algorithms to complete the filtering process fast. The HLT reduces the event rate from 100 kHz to 100 Hz. A set of trigger paths forms the HLT menu, one or any combination of trigger paths are selected for filtering the events relevant to the physics studied [11]. Finally, the events passed the HLT farm are reconstructed offline and are written to disks.

CHAPTER 4

THE HF MISALIGNMENT

The HF has been designed as rotational symmetric with respect to collision vertex. Owing to symmetry, energy response of $i\phi$ cells for each ring are equalized. This is called as azimuthal symmetry correction. However, misalignment of the HF breaks the azimuthal symmetry, and this leads the measurement to be unreliable. This chapter focuses on the misalignment effects in the HF.

4.1 The Calibration

The Hadronic Forward calorimeter has a composite structure that composed of iron for showering, and quartz fibers transmit the Cherenkov light to the PMTs where light is converted to the electronic signal corresponds to energy deposition of incoming particle. The measured quantity is current and to get the deposited energy of incoming particle, it is needed to find a relation between the current and the energy. This is the first step of calibration. Because energy depends on current linearly, the relation takes the form;

$$E = C(A - A_0) \tag{4.1}$$

where E is the energy, C is a calibration constant, A is the signal current and A_0 is the current measured when there is no collision.

Before CMS assembly, this calibration was done to limited number of HF modules with test beams in order to get reference calibrations. After the assembly, the remaining detector modules is calibrated with respect to reference calibrations by gamma rays generated by Co^{60} radioactive sources. The results taken

from these calibration techniques show that detectors are calibrated with only 7% accuracy [13]. Despite low accuracy of the calibration techniques mentioned above, the results provide good reference for the energy response of the detector and this process is called precalibration.

The main goal of the HCAL calibration is to create a reproducible hadronic energy scale and to perceive the detector response and uniformity. Because the conditions such as radiation and magnetic field are not same for all modules of the detector, response of the detector is affected. Therefore, additional calibration techniques are needed to be applied while collision takes place to achieve the main goal.

There are two major parts of the calibration:

- Relative correction: equalize energy response of HF cells in rings of constant η;

- Absolute correction: equalize energy response of HF cells by using Z$\rightarrow$ee events;

First part of the calibration, azimuthal symmetry correction, uses the advantage of cylindrical structure of the detector and ϕ symmetric energy distribution of produced particles. The total energy deposited in iϕ cell of constant iη ring should be uniform if center of the ring sits on beam axis and by using this equality detector cells are calibrated relatively. This calibration method is used for all of the calorimeter sub-detectors. Result of the ϕ symmetry calibration is used in absolute scale correction. Due to fact that tracker coverage does not exist in the forward region, HF long fibers are calibrated by using high energy resolution and position resolution of the ECAL. For this purpose Z$\rightarrow$ee events with decay products that deposit their energy in ECAL and HF respectively, are chosen. Afterwards, short fibers are calibrated with Monte-Carlo estimated energy ratio between long and short fibers.

4.1.1 Azimuthal Symmetry

Azimuthal (ϕ) symmetry is the first step of the HF calibration with collision data. This method uses rotational symmetry of the detector and azimuthal symmetry of event activity that need to be the same at certain pseudorapidity (η). The HF is composed of 13 nested rings, each designed to correspond to certain η. Each ring divided into 36 cells (except $|i\eta|$=40 and $|i\eta|$=41 ring, which have 18 cells) and the cells of a particular ring are calibrated relative to others.

Two different calibration methods; iterative method and method of moments, are performed to adjust ϕ symmetric energy response of the HF [14]. Iterative method uses any physics data between some thresholds that correspond to upper limit of the noise and lower limit of PMT hits. Method of moments uses min-bias events that include all the data of a typical p-p collision. Aim of the both method is to equalize the energy response of the cells to the mean of energy distribution in the ring. They use different approaches to get better corrections.

4.1.1.1 Iterative Method

Any physical data stream can be applied for iterative method. However events not depend on HCAL triggers should be chosen to get better results. Hits below the pedestal tail are taken into account and hits above certain energy level are cut, in order to avoid PMT hits.

Energy threshold is determined regarding the sub-detector calibrated. While E_{low} is 10 GeV and E_{high} is 150 GeV for the HF, E_{low} and E_{high} are chosen 4 GeV and 100 GeV, respectively, for HE.

Total deposited energy on the cell is not computed directly. First, spectrum dN/dE is calculated from energy distribution, than total energy is evaluated from the spectrum. Relation between total energy and spectrum is given as;

$$E_{tot} = \int_{E_{high}}^{E_{low}} \frac{dN}{dE} E dE \tag{4.2}$$

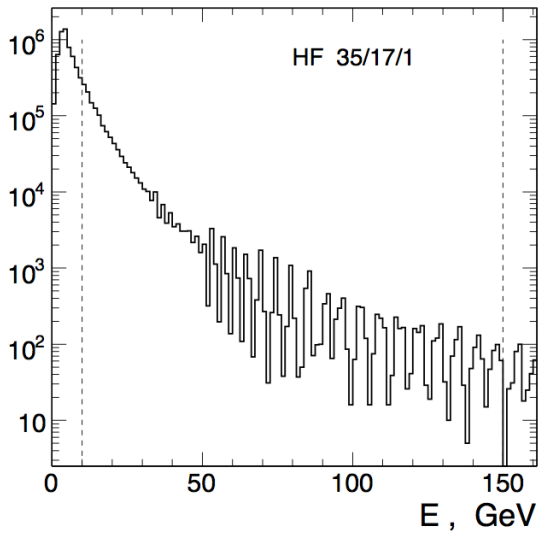

Figure 4.1: Energy spectrum for HF iη=35, ϕ=17 channel. Energy limits are demonstrated with dash lines.

Energy response of the cell is adjusted by equalizing E_{tot} to the average energy of the ring. However, each total energy is not simply multiplied by a correction factor. A change in total energy of a cell affects average energy of the ring and total energy is found in iterations.

4.1.1.2 Method of Moments

In method of moments, the correction coefficients are calculated using the first two central moments of deposited energy distribution, which are mean and variance [17]. Central moments of a cell are compared with average central moments in entire ring and come up to them. The correction coefficient for each cell by using mean is given by;

$$C_{i\eta i\phi} = \frac{\frac{1}{N_{i\phi}} \sum_{i\phi} (< E_{i\eta i\phi} > - < E^{noise}_{i\eta i\phi} >)}{< E_{i\eta i\phi} > - < E^{noise}_{i\eta i\phi} >} \tag{4.3}$$

where $N_{i\phi}$ is the number of cells in a particular ring and the mean of deposited energy in the cell can be expressed $< E_{i\eta i\phi} >=< E^{signal}_{i\eta i\phi} > + < E^{noise}_{i\eta i\phi} >$ For non-zero suppressed minimum bias data $< E^{noise}_{i\eta i\phi} >= 0$ (Figure 4.2), The correction coefficient becomes;

$$C_{i\eta i\phi} = \frac{\frac{1}{N_{i\phi}} \sum_{i\phi} < E_{i\eta i\phi} >}{< E_{i\eta i\phi} >} \tag{4.4}$$

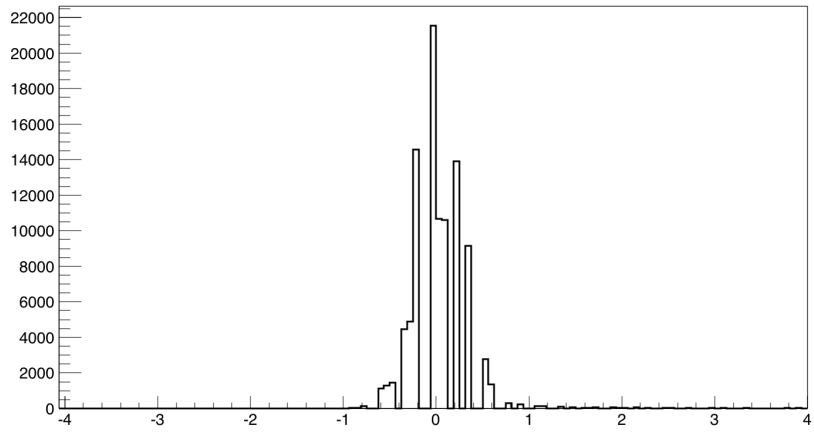

Figure 4.2: Pedestal sample for HF iη=36, ϕ=19 channel with 100000 events.

Even though mean of the pedestal is zero, variance of the pedestal does not vanish. Moreover, variance analysis is necessary for detailed investigation of correction factor. The correction coefficient for the second central moment is expressed as follows;

$$C_{i\eta i\phi} = \sqrt{\frac{\frac{1}{N_{i\phi}} \sum_{i\phi} (< V_{i\eta i\phi} > - < V^{noise}_{i\eta i\phi} >)}{< V_{i\eta i\phi} > - < V^{noise}_{i\eta i\phi} >}} \tag{4.5}$$

Due to fact that energy distribution of particles for a particular η is constant at the interaction vertex, mean of the deposited energy for all cells in a particular ring is assumed to be equal. However, the ring is assumed to locate between constant η values, the particle distribution is not ϕ symmetric owing to magnetic field and the amount of dead material in front of the cell. Effect of inhomogeneous magnetic field is small and can be neglected. However inhomogeneity in material structure affects ϕ symmetrical behavior of energy deposition. Regardless of the magnetic field, noise and effect of the material, the central moments is defined as;

$$< x_i >= \int_0^E x f(x) dx \tag{4.6}$$

$$< x_i^2 >= \int_0^E x^2 f(x) dx \tag{4.7}$$

Considering the mentioned effects, central moments become;

$$< x_i >= \int_{a_i}^E x f(x) dx \tag{4.8}$$

$$< x_i^2 >= \int_{a_i}^E x^2 f(x) dx \tag{4.9}$$

where f(x) is energy spectrum and a_i, minimum detectable energy, is equal for all cells if the amount of material in front of the cells are the same. The effects also create small differences between correction factors evaluated using mean and variance of energy deposition.

Final calibration coefficients are evaluated by computing the error-weighted average of the corrections coming from the iterative method and method of moments. Iterative method deals with more energetic hits compared to method of moments. Therefore, two azimuthal symmetry inter-calibration methods complement each other to cover wider energy range and to get better energy response.

4.1.2 Absolute Scale Calibration

After cells in a constant iη ring calibrated relatively, energy response of the rings need to be calibrated with respect to reliable source. Z→ee events with one daughter electron depositing its energy to the ECAL and the other daughter electron going to the HF are chosen for this purpose.

Z boson is very massive ($m_Z = 91.1876 \pm 0.002 GeV$) and its mass is precisely known [15]. The high mass of the Z boson makes the angle between daughter particles very large. Therefore, the probability of daughter electrons with one electron absorbed in the ECAL and with other electron ending up in the HF, is high. The reason to select the ECAL as a reference detector is its high position and energy resolution. Despite 3% branching ratio of Z→ee, daughter electrons

can be easily detectable. This is the other reason why Z→ee is chosen instead of other decay modes. The HF absolute energy scale is adjusted by comparing

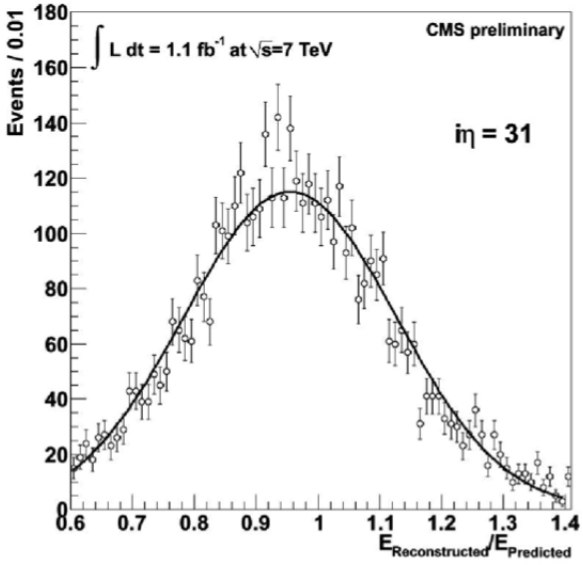

Figure 4.3: The ratio of reconstructed and predicted energy deposition on HF iη=31 ring.

reconstructed energy with expected energy and the ratio between them gives the correction coefficient. As it can be seen in Figure 4.3, the ratio data is normally distributed and the mean of the Gaussian distribution equals to the one over correction factor. The expected energy of the HF electron can be calculated as follows;

$$E_{HF} = \frac{m_Z^2 \cosh \eta_{ECAL} \cosh \eta_{HF}}{2E_{ECAL}(\cosh(\eta_{ECAL} - \eta_{HF}) - \cosh(\phi_{ECAL} - \phi_{HF}))} \tag{4.10}$$

As it is seen from the equation, energy of the HF electron depends on mass of Z boson, energy and position of the ECAL electron. Fortunately, they are all well known. However, it also depends on the HF electron position and it is considered that position of the HF is misaligned [18]. In next section effect of the misalignment will be discussed.

4.2 Misalignment of the HF

According the studies conducted, energies of outgoing particles measured from the HF shows some inconsistencies. Therefore, alignment of the HF is suspected to be wrong. Due to cylindrical and compact structure of the HF, reason of the misalignment should be the shift of its center. The compact structure of the CMS does not allow measuring the defect of the HF skeleton by any displacement sensor. Because of that reason, Amount of the shift is not known. This study focuses on variation in the total energy deposited in the HF due to shift of its center.

The effect of the shift on alignment of readouts and the reasons of the change in total energy deposition are discussed in the following sections.

4.2.1 Effects of the Shift on Alignment of the Readouts

Each readout channel of the CMS detector corresponds to a particular iη and iϕ values. Due to granular structure of the CMS, $i\phi$ and $i\eta$ are discrete forms of the ϕ and η respectively; and remain between particular interval of ϕ and η. Real position of the outgoing particle within a margin of error can be determined by using various methods. However, if corresponding ϕ and η values are known incorrectly, the position of the outgoing particle is mismeasured.

Due to η = -ln(tan $\frac{\theta}{2}$) and $\theta = \frac{r}{z}$, where r is the distance from beam axis to a point on the HF and z is position of the HF on the beam axis. After shift by s mm in x direction, Change in the η of any point on the HF can be calculated as follows;

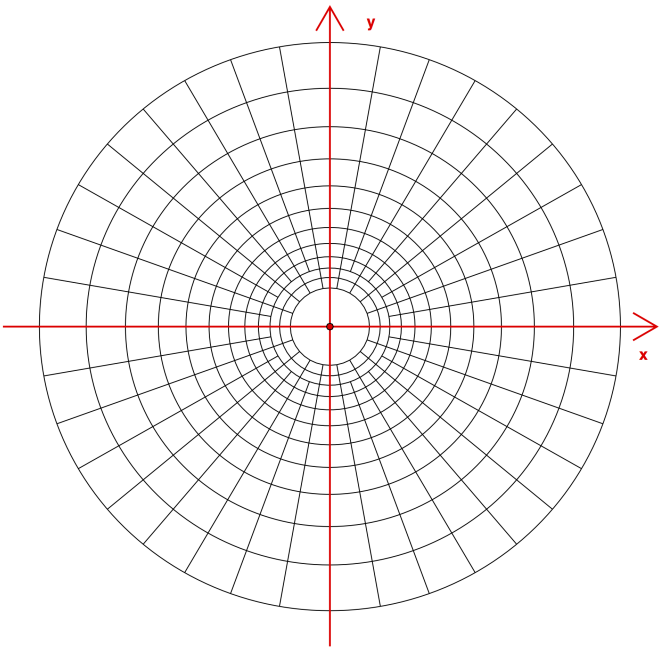

(a) Ideal case.

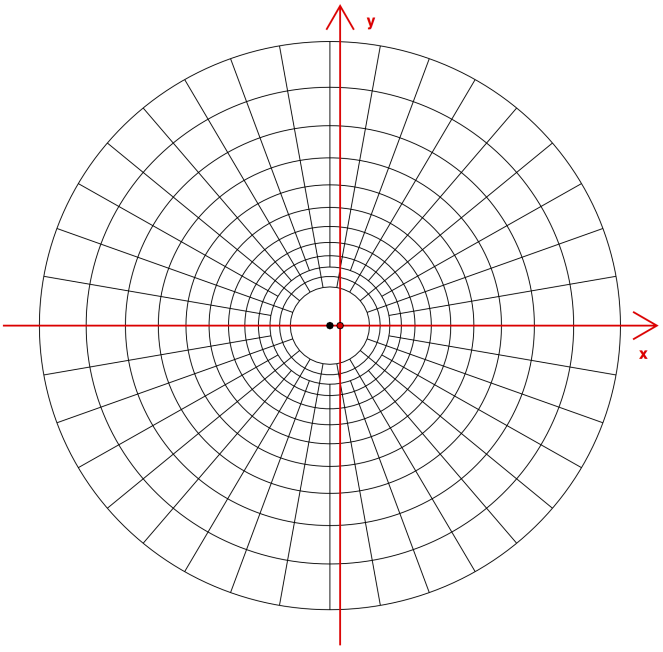

(b) Shifted in -x direction case.

Figure 4.4: Schematic front view of the HF; top shows ideal case and bottom shows shifted geometry.

$$x \to x + s \quad \text{and} \quad r \to R$$
$$R = \sqrt{(x+s)^2 + y^2}$$

Because $x = r\cos\phi$ and $y = r\sin\phi$

$$R = \sqrt{r^2 + s^2 + 2rs\cos\phi}$$

and,

$$\theta \to \theta' \quad \text{and} \quad \theta' = \arctan(\frac{R}{z})$$

η becomes;

$$\eta(r, \phi, s) = -\ln[\tan(\frac{1}{2}\arctan(\frac{\sqrt{r^2 + s^2 + 2rs\cos\phi}}{z}))] \tag{4.11}$$

Now η is ϕ and s dependent. It means that η is not invariant for the constant iη HF ring. If s is unknown, assumed η is not true η. New η values are calculated for the HF rings for 10 mm shift in x direction. Below, iη 41 and iη 30 rings' η values before and after shift are shown.

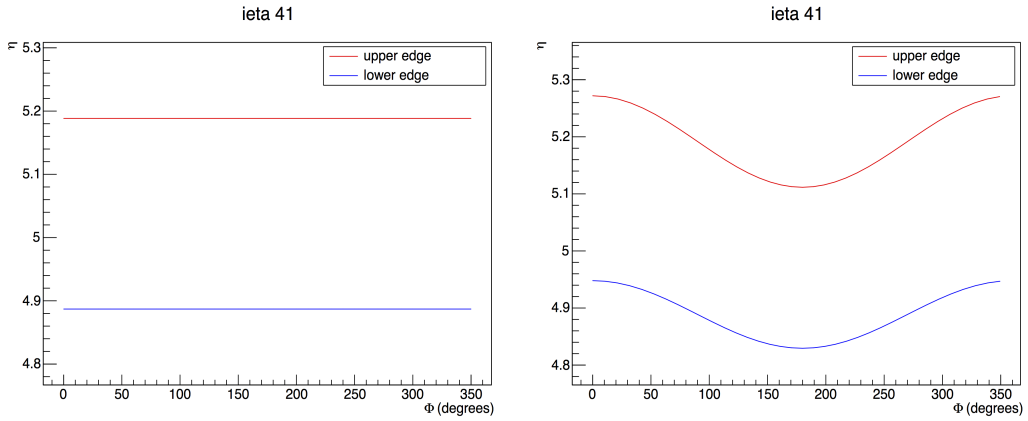

(a) Ideal case.

(b) Shifted in -x direction case.

Figure 4.5: η values for edges of the HF $i\eta$=41 ring.

Because iη 41 ring is the closest ring to beam axis, it is the most affected ring from the shift in η aspect.

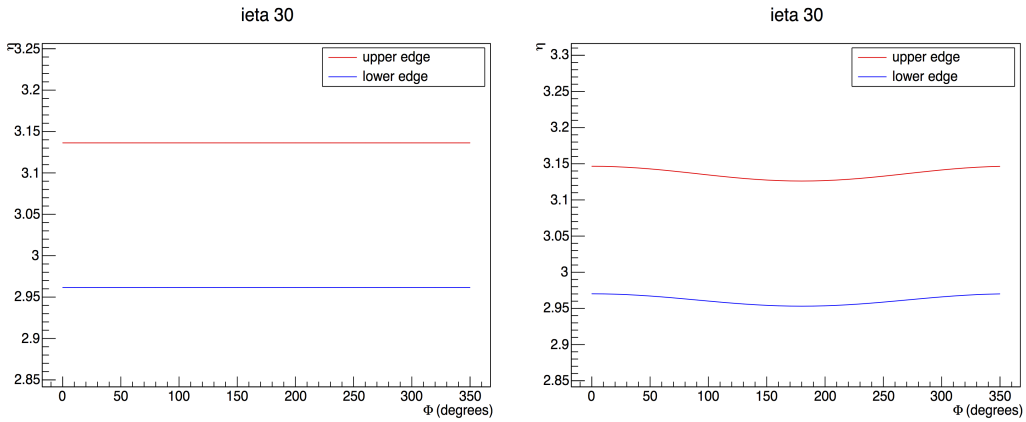

(a) Ideal case.

(b) Shifted in -x direction case.

Figure 4.6: η values for edges of the HF $i\eta$=30 ring.

Outermost ring's variation in η is about 10 times less than iη 41's variation. Energy spectra of the outgoing particles is ϕ independent and it depends on η. Therefore, any variation in η leads the change of energy deposition in readouts. More detailed discussion will be conducted in the following section.

As stated before, rings from iη 30 to iη 40 there are 36 readouts, and ϕ interval of the readouts are 10°. ϕ interval of the readouts on the last innermost rings are 20°, so they have 18 readout channels. Even though each ring is divided equally by readouts, shift of the HF affects ϕ intervals of the readouts. Total energy deposited on any readout depends on the angle measured from x axis. While total energy are calculated from the energy density, a change in the ϕ interval should be taken into account.

Analytically, a change in the ϕ interval after the shift can be calculated as follows;

$$\phi' = \arctan \frac{y_1}{x_1 + s}$$
$$\tan \Delta\phi' = \frac{y_2}{x_2 + s} - \frac{y_1}{x_1 + s}$$
$$\Delta\phi' = \arctan \frac{y_2(x_1 + s) - y_1(x_2 + s)}{(x_1 + s)(x_2 + s)}$$

where (x_1, y_1)=$(r\cos\phi, r\sin\phi)$ and (x_2, y_2)=$(r\cos(\phi + \Delta\phi), r\sin(\phi + \Delta\phi))$

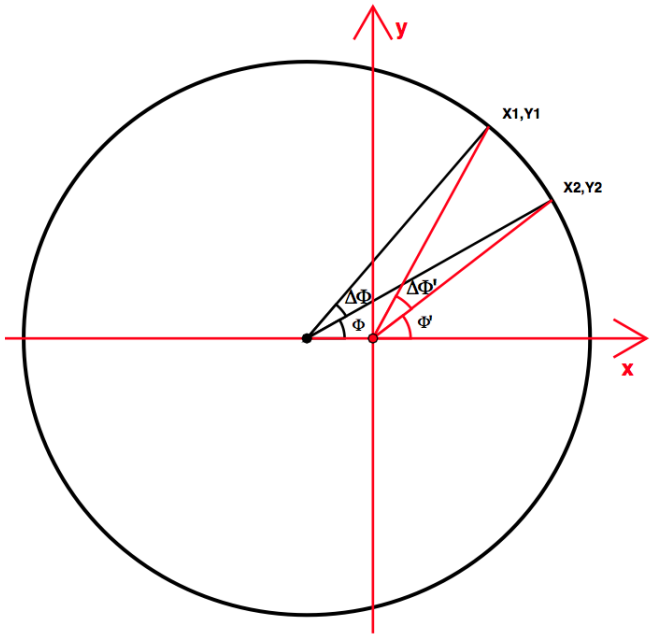

Figure 4.7: Schematic view of ϕ interval before and after the shift.

A change in the ϕ interval after 10 mm shift in x direction are shown below and, it is expected that innermost ring is the most affected.

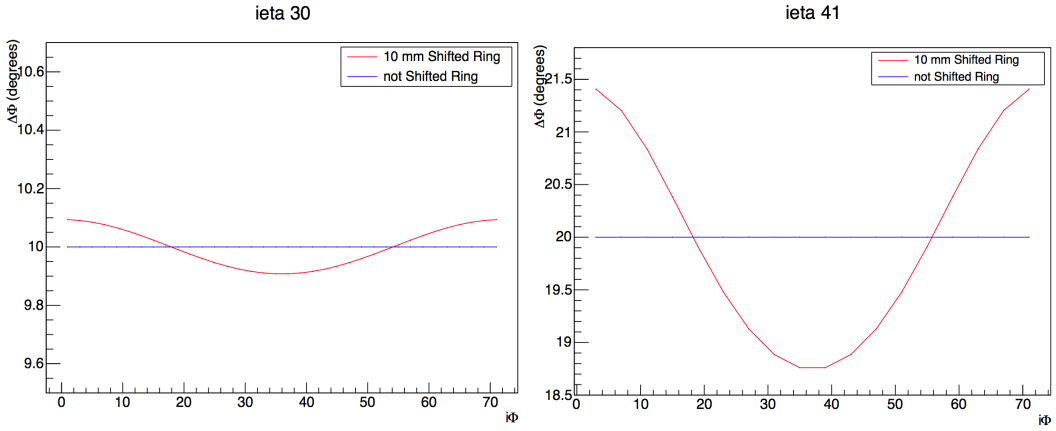

(a) $i\eta$=30 ring (b) iη=41 ring.

Figure 4.8: ϕ interval of readouts before and after the shift.

Due to fact that distance of the each readout to collision point is changed after the shift, solid angle of the readouts are also changed. A change in the solid angle affects number of particles hit the readouts and this causes variance of the

total energy deposited on readouts. Solid angle (Ω) is defined as ;

$$\Omega = \sum_{i=1}^{N} \frac{A_i}{{r_i}^2} \tag{4.12}$$

where any readout is divided N equal infinitesimal areas.

In order to understand the deflection of solid angle, solid angle of the readouts on any ring is normalized to 1. As shown below Solid angle of low iη rings' readouts are much more affected by shift. However maximum change is about 0.015%. A change in solid angle after 10 mm shift affects total energy deposition negligibly. Therefore, Change of the energy spectrum causes variance of the total energy deposited on readouts.

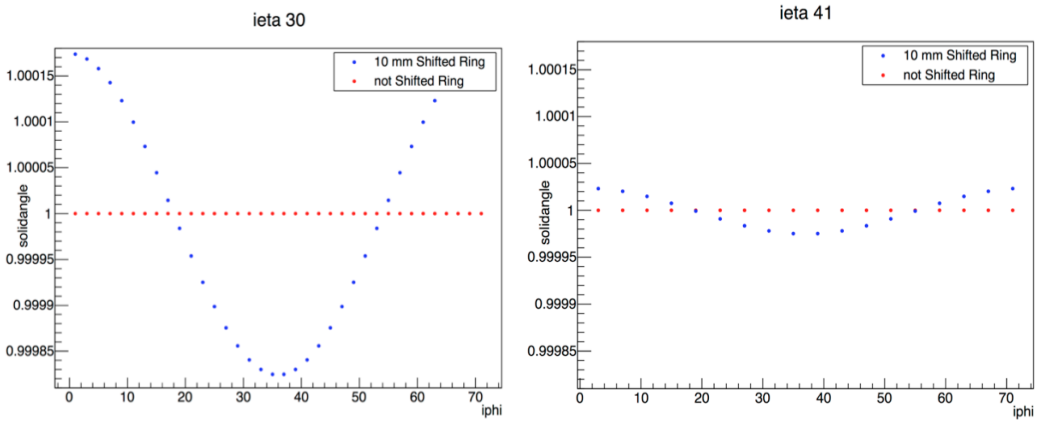

(a) $i\eta$=30 ring. (b) iη=41 ring.

Figure 4.9: Solid angle of the readouts before and after shirt.

4.2.2 Study of misallignment effects in the CMS Hadron Forward Calorimeter

ϕ symmetry calibration is the first step of situ-calibration and uses azimuthal symmetry of total energy deposition that need to be equal at each η. If the center of the HF has not been shifted from its ideal position, its nested rings would be in true η, and ϕ calibration would be valid. However, an unknown shift makes this method ineffective.

In this study, change in total deposited energy in HF is analyzed in case of 10

mm shift in x direction. In order to achieve this, two different Monte-Carlo data sets which have the same generator objects have been produced. While collision point of the first data set is at origin of the CMS coordinate system, the collision point of the other data set is shifted 10 mm in positive x direction in order to mimic 10 mm HF shift. The paths of the data sets are given below;

- QCD_Pt-15to7000_TuneCUETP8M1_Flat_13TeV_pythia8 /Fall14DR-NoPU_NZS_MCRUN2_72_V3-v1/ GEN-SIM-RECO
- QCDJets_flat_pythia_shiftedvertex/Fall14DR-NoPU_NZS_Shifted Collision2015_MCRUN2_72_V3-v1/ GEN-SIM-RECO

First, data sets at center of mass energy $\sqrt{s}$=13 TeV is analyzed at the generator level. Then, reconstructed objects are analyzed to understand the deflection of the total energy. In order to express the analyses more clearly it would be better to explain Generator level and Reconstruction level objects.

Generator level, produced using particle generator programs such as Pythia or Herwig++, is the first step of the Monte-Carlo event simulation chain. Generator level objects are the outgoing particles from a proton-proton collision and consist of particle identity(such as photon, electron, pion, etc...), four-momentum, charge and particle position information. The important point is that they are just the particles themselves and there are no detector effects or any extrinsic factors in the data.

Once the particles have been generated, particle passage and interactions in the detector medium are simulated. This process is composed of several steps and steps can be different with respect to simulation methods. The last step is the reconstruction level and it is the total simulation of the signals generated by detector components of the CMS after collision.

Reconstructed level objects do not consist of particle ID, momentum, charge or energy as data members . They are only electric signal which represent energy deposition for calorimeter and from the readout number, discrete position of the signal is identified. Energy signal is the total energy deposition on readout at a bunch crossing. Therefore, it can be energy deposition of many particles or

only noise. By using several software methods and hardware triggers particle information is determined. However, particle identification is not possible for min-bias events which mean no physical trigger. As stated before, min-bias data is used for only calibration purposes, not for physics studies.

4.2.2.1 Generator Level Study

Generator level study has been conducted using position and energy information of generator objects. Since position of the HF readouts are defined, total energy of the particles passing through the readouts per bunch crossing can be determined. Using geometrical relations stated before, position of the readouts after 10 mm shift in x direction can be calculated and total energy of the particles passing through shifted readouts is determined. In this study, there is no particle detector interaction and noise. That is, particles hit the detector do not make shower. Therefore, all of their energy belongs to readouts where they hit.

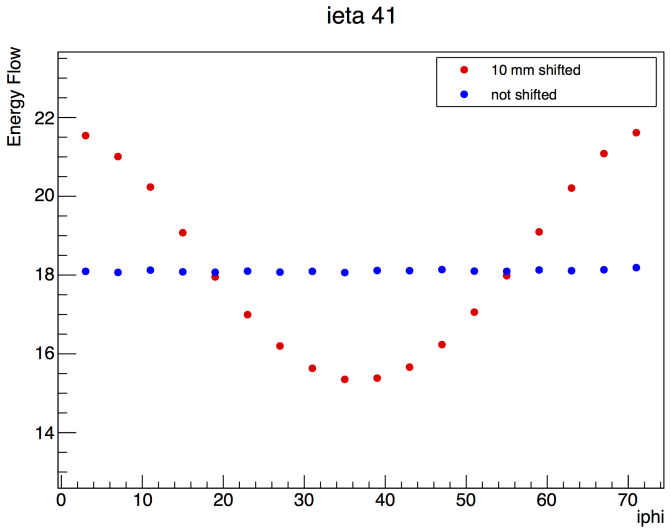

Figure 4.10: Energy deposition on HF iη=41 ring in the case of 10 mm shift and no shift.

As it is seen from the figure above, uniformity of the total energies of the particles passing through the readouts are affected after 10 mm shift. A shift in the HF causes to change the energy spectrum in the HF aperture. The total energy is minimum at the readouts farthest from beam line and maximum otherwise. High $i\eta$ rings are affected much more than others. However, energy flows for

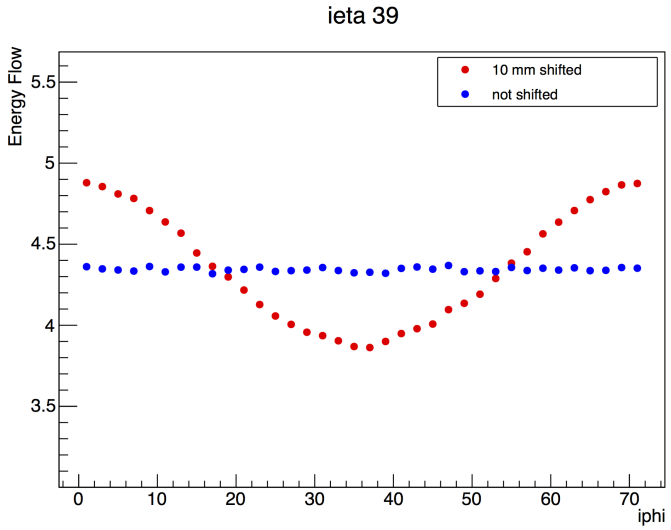

Figure 4.11: Energy deposition on HF iη=39 ring in the case of 10 mm shift and no shift.

low $i\eta$ rings are almost uniform because effect of 1 cm shift on the η values of the rings with about 100 cm radius is small.

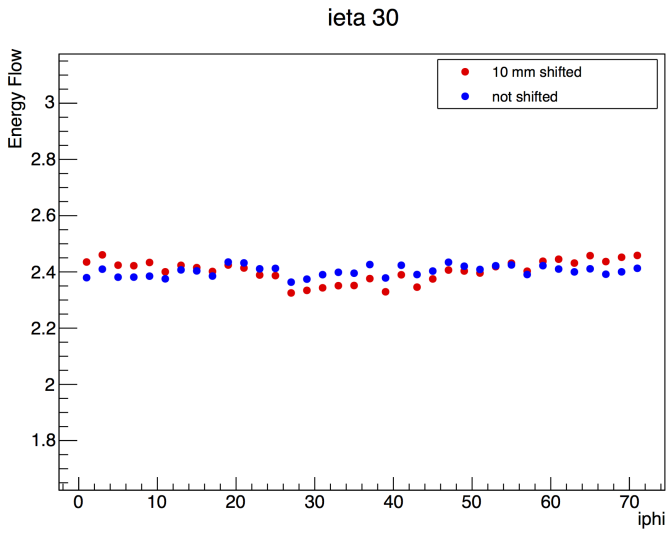

Figure 4.12: Energy deposition on HF iη=30 ring in the case of 10 mm shift and no shift.

As stated before, a change in the solid angle after 10 mm shift does not affect the total energy deposition in readouts. The main reason of change in the energy deposition is the shift of energy spectrum in HF aperture. Because event activity is azimuthal symmetric, change of the energy spectrum is only caused by a change in the η from ideal case. Even though η values of readouts change,

average η value of the rings do not change much. Therefore, total energy flow per ring should be almost not affected due to 10 mm shift. Total energy flow for the shifted case and not shifted case are shown in Figure 4.13.

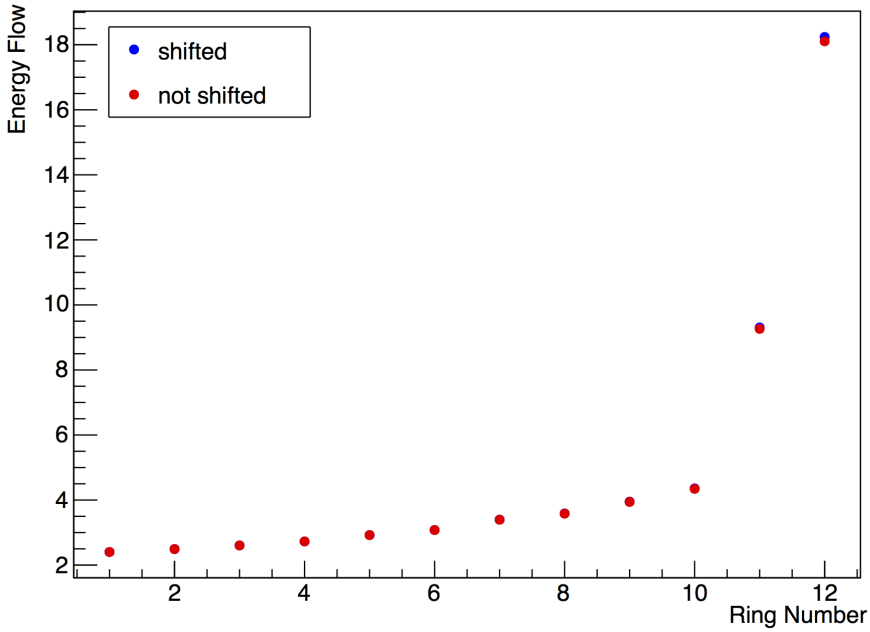

Figure 4.13: Average energy flow per ring.

As it can be seen from the energy flow versus iϕ plots above, energy flow is not uniform after the shift, and its behavior can be parametrized in terms of radius. Since the HF provides 2-dimensional spatial identification, energy density can be easily expressed as energy flow per unit area. Energy density as a funtion of radius and Landau distribution function that is fitted to data are shown in fugure 4.14.

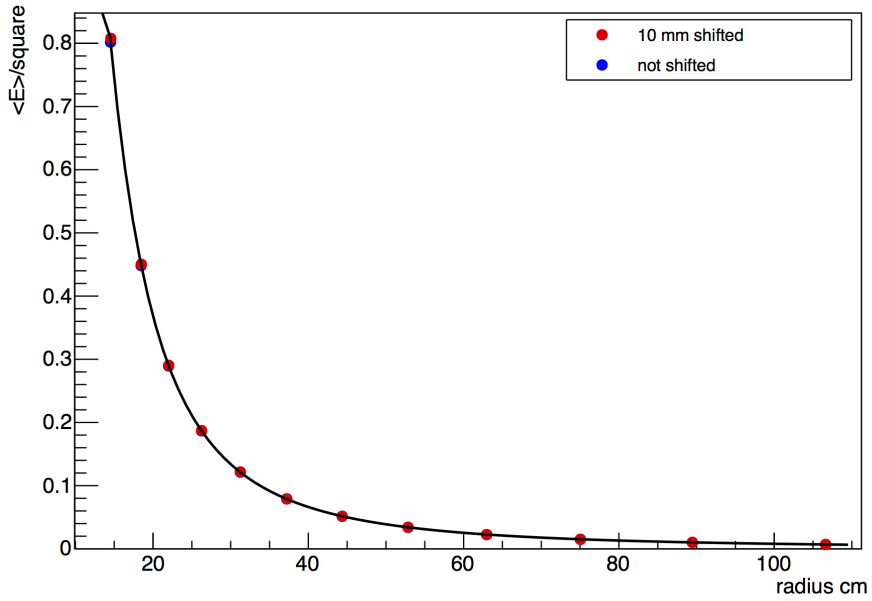

Figure 4.14: Energy density on the HF plane and Landau distribution function is fitted to the data.

Landau function can be expressed as follows;

$$Landau(R) = Par(3) * Moyal(\lambda) \tag{4.13}$$

where $\lambda = \frac{R-m}{s}$, m and s are Par(1) and Par(2), respectively. Parameters are determined by MINUIT which is minimization package in the ROOT.

$$Moyal(\lambda) = \frac{e^{-0.5*(\lambda+e^{-\lambda})}}{\sqrt{2\phi}} \tag{4.14}$$

While calculating total energy flow, it is better to transform coordinate system from beam axis to center of the HF in order to use equal ϕ intervals.

$$(R, \phi') \rightarrow (r, \phi)$$

The relation $R = \sqrt{r^2 + s^2 + 2rs\cos\phi}$ is enough for calculation since the area element is equal for both systems. Then, total energy per readout is calculated as follows;

$$E_j(\phi_i, s) = \int_{\phi_i - \frac{\Delta\phi}{2}}^{\phi_i + \frac{\Delta\phi}{2}} \int_{R_{j-1}}^{R_j} L(r, s, \phi) r dr d\phi \tag{4.15}$$

where ϕ_i is the mean angle of the readout and $\Delta\phi$ represents ϕ_i interval of the readout. Moreover, i and j are readout number and ring number, respectively.

Using equation 4.15 , total energy flows per readout have been calculated in case of 10 mm shift. The parameterized energy flow and energy flow from Monte-Carlo are shown together in the Figures 4.15 and 4.16.

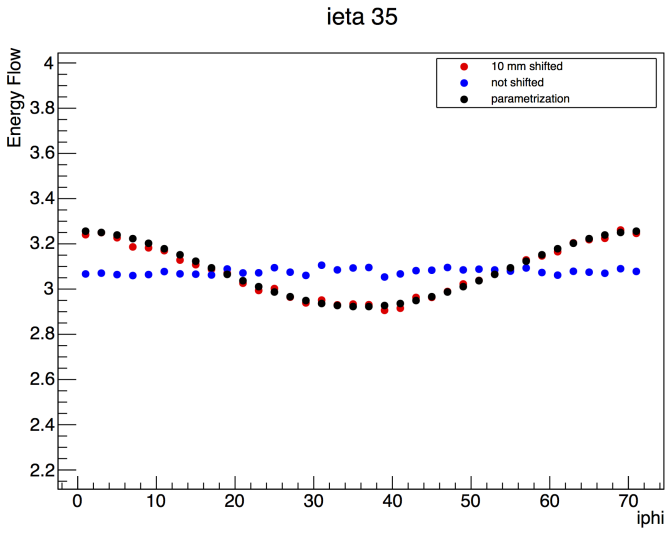

Figure 4.15: Calculated energy deposition and simulated energy deposition for the HF $i\eta$=35 ring.

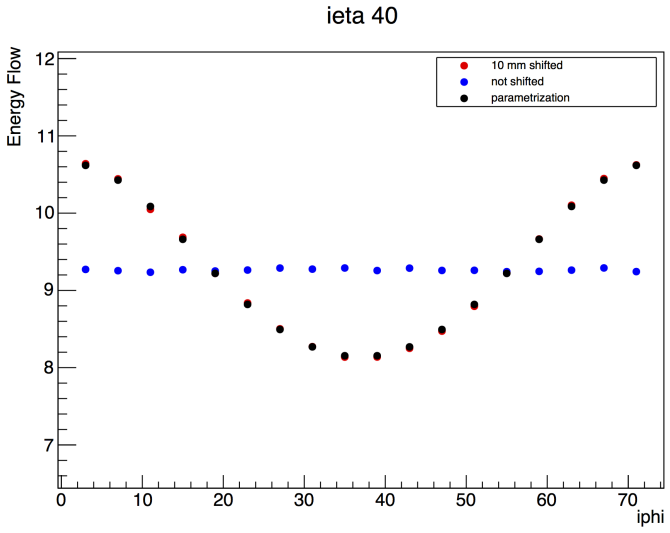

Figure 4.16: Calculated energy deposition and simulated energy deposition for the HF $i\eta$=40 ring.

In order to analyze how well the model reflects the data, it is good to make a

statistical test. Generally for this purpose chi-square test is applied. Chi-square is a value which gives the quality of the model and it can take any value between zero to infinity. When the value approaches to zero, the model approaches to perfect fitness.

Chi-square is expressed as follows;

$$\chi^2 = \sum_{ring} \sum_{readout} \frac{(E_{observed} - E_{expected})^2}{E_{expected}} \tag{4.16}$$

Because Landau distribution function fitted to energy density values calculated from not shifted HF case. Expected energy values have been calculated from not shifted to 20 mm shifted in 1 mm increments. χ^2 values using these expected values and total energy flow for 10 mm shifted case shown in figure 4.17.

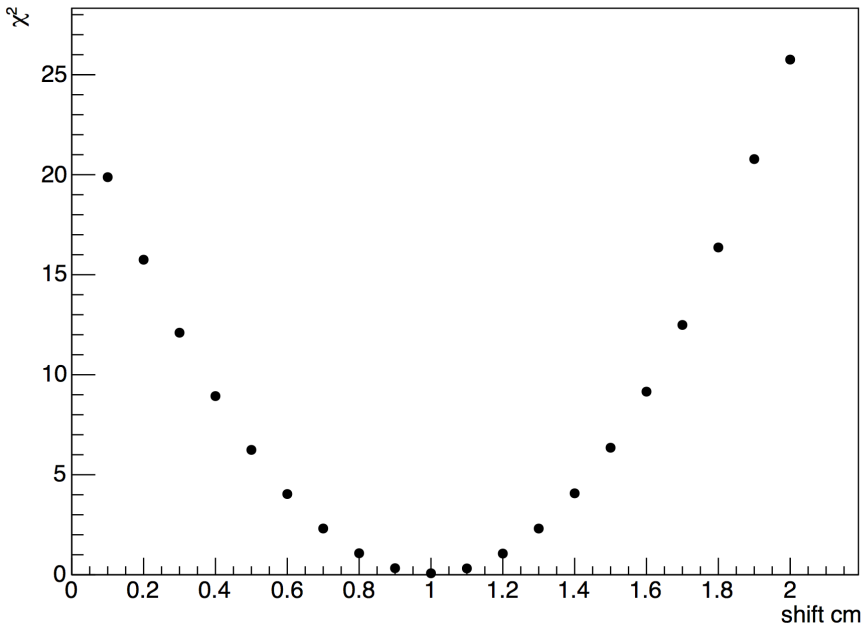

Figure 4.17: χ^2 vs shift graph; reaches minimum at 1 cm.

As seen in the figure 4.17, minima of χ^2 is at 10 mm shift and it is very close to zero, this means that the model perfectly fits the data.

4.2.2.2 Reconstruction Level Study

As stated before, reconstruction objects only consist of total energy deposition per bunch crossing and readout addresses. Using these information, energy deposition versus $i\phi$ distributions are obtained. As they are seen in the figure 4.18, energy deposition in HF+ and HF- differ little due to different z positions. However, the distribution shapes look similar. This means that external effects on HF+ and HF- are quite same.

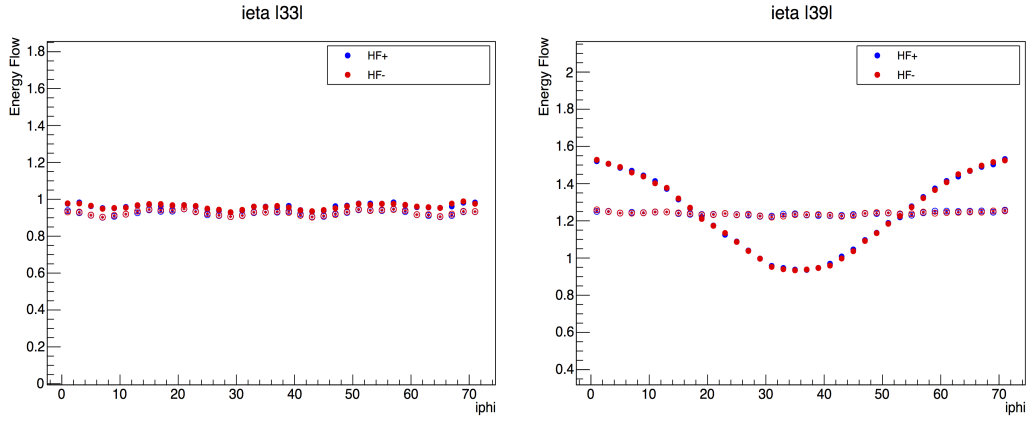

(a) $i\eta$=33 ring. (b) iη=39 ring.

Figure 4.18: Energy deposition in HF+ and HF- in case of 10 mm shifted and not shifted.

In order to parametrize the energy deposition, two Landau functions are fitted to the distribution of the energy density. The fitted function is;

$$f(R) = \begin{cases} Par(3)\frac{e^{-0.5*(\frac{R-Par(1)}{Par(2)}+e^{-(\frac{R-Par(1)}{Par(2)})})}}{\sqrt{2\phi}} & \text{if } 10 < R < 48 \\ Par(6)\frac{e^{-0.5*(\frac{R-Par(4)}{Par(5)}+e^{-(\frac{R-Par(4)}{Par(5)})})}}{\sqrt{2\phi}} & \text{if } 48 \leq \text{R} \end{cases} \tag{4.17}$$

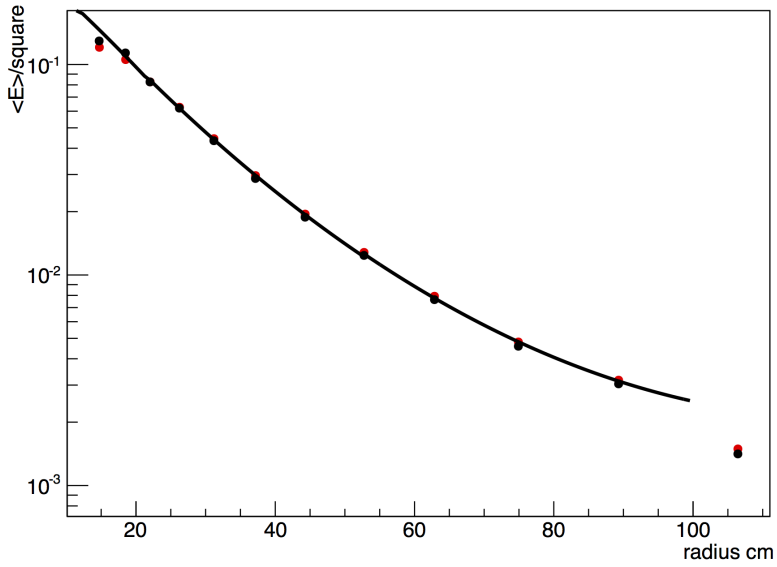

Figure 4.19: Energy density in the HF plane and two landau functions fit the MC data.

Deposited energy on readouts have been calculated by using the fit function. As it can be seen in energy flow versus $i\phi$ distributions, parametrization works well for low $i\eta$ rings. However, calculated energy flows do not fit very well for high $i\eta$ rings.

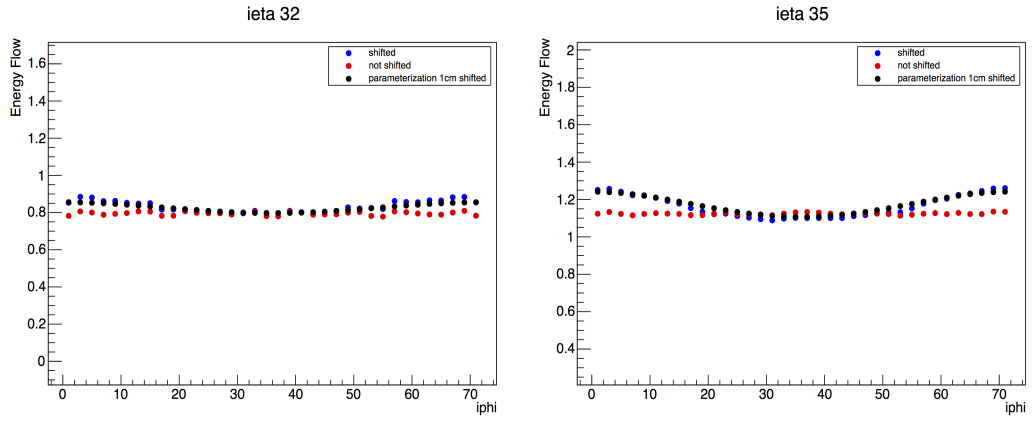

(a) $i\eta$=33 ring (b) iη=39 ring

Figure 4.20: Calculated energy deposition and simulated energy deposition in both cases.

Energy flows for high $i\eta$ rings are much more affected than expected. Moreover, sinusoidal shapes are degenerated. Since degeneration is sharp for $i\eta$ 40 and 41

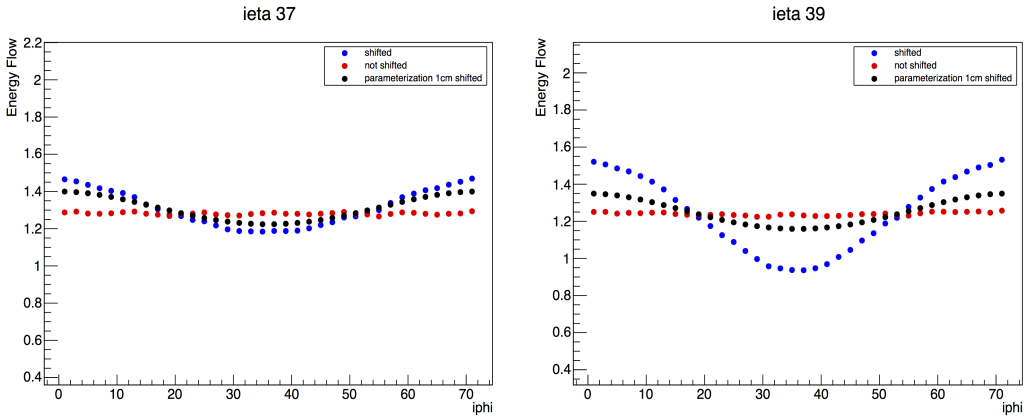

(a) $i\eta$=33 ring (b) iη=39 ring

Figure 4.21: Calculated energy deposition and simulated energy deposition in both cases.

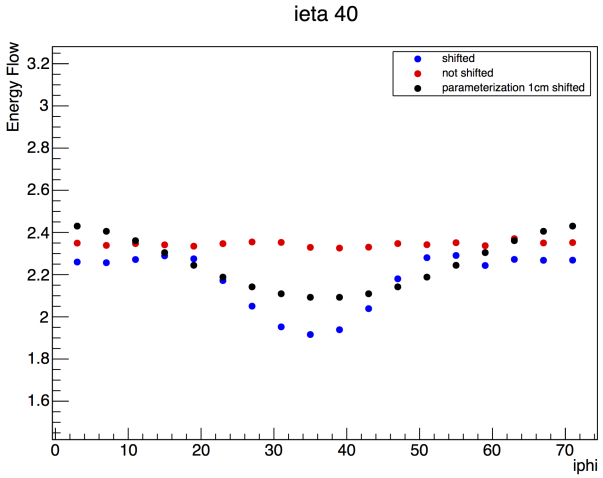

Figure 4.22: Calculated energy deposition and simulated energy deposition on HF $i\eta$=40 in both cases

rings, they are excluded from χ^2 calculation. In this case, χ^2 has the minimum value at 1.25 cm . This means that shift value is needed to be chosen as 1.25 cm in order to explain 1 cm shift. However, fittingness of the model for low $i\eta$ rings diminish in this case. The model only depends on geometrical effects and it states that shape of the energy flow should be sinusoidal and total energy per readout should be invariant under the shift. However, as it is seen in Figures 4.24 and 4.22 variation in the energy flow does not only depend on geometrical defects. More detailed study is needed to identify the other effects and integrate them into the model.

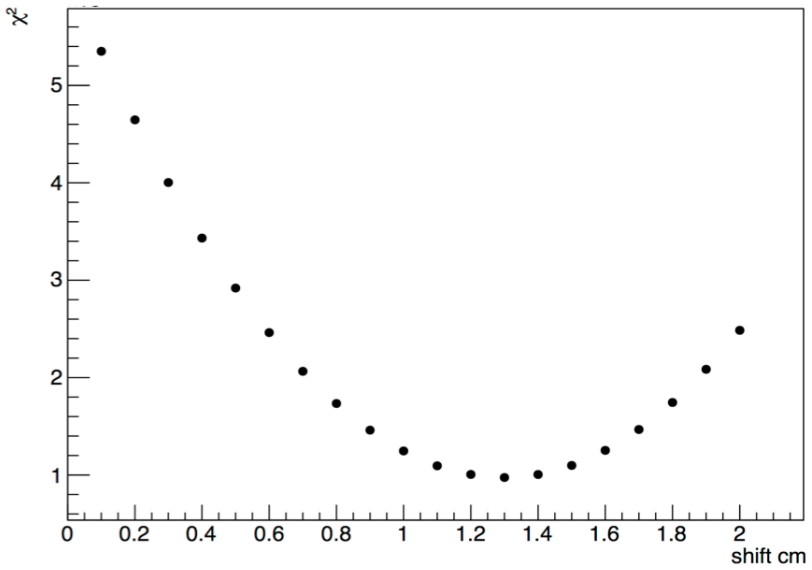

Figure 4.23: χ^2 vs shift graph; reaches minimum at 1.25 cm.

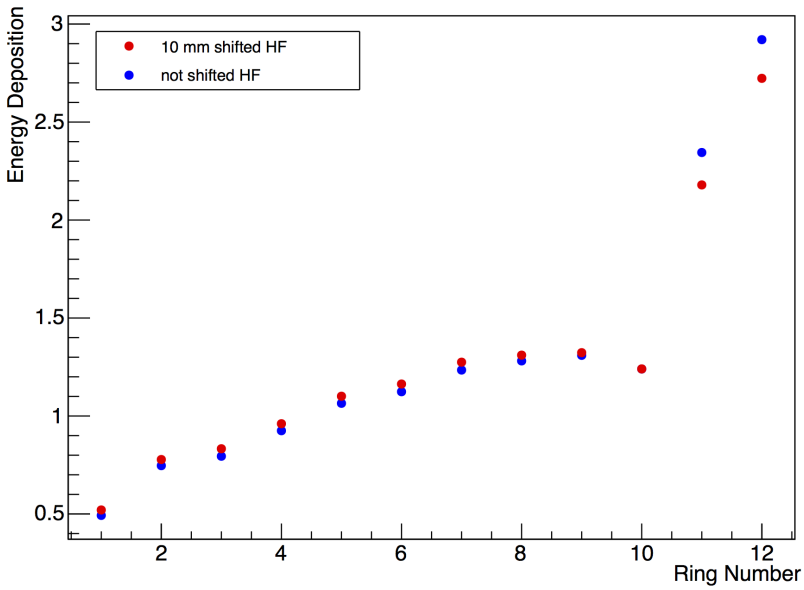

Figure 4.24: Average energy deposition per ring

CHAPTER 5

CONCLUSION

Azimuthal symmetry correction is the first step of situ calibration used to regulate energy response of the HF. This method uses the advantage of rotational symmetry of the detector and azimuthal symmetric energy distribution of outgoing particles. By using uniformity of total energy deposition in $i\phi$ cells on a certain $i\eta$ ring, energy responses of the cells are calibrated relatively. Azimuthal symmetry is useful if only center of the HF sits on beam axis. In case of shift of the center, alignment of the readouts is affected and this causes to ruin uniformity of total energy deposition in the readouts. This study, simulation based, focuses on effects of 10 mm shift of the HF on total energy deposition in x direction.

As stated in Chapter 4, position of the readouts are defined in terms of $i\eta$ and $i\phi$. $i\eta$ and $i\phi$ are addressed between particular interval of η and ϕ, respectively. After the shift, η and ϕ values of the readouts changed. New η values are calculated for the HF rings in case of 10 mm shift in x direction. Closest rings to beam axis are the most affected in η aspect. Despite the fact that each ring is separated equally by readouts, $\Delta\phi$ size of the readouts change due to the shift. New $\Delta\phi$ sizes are also calculated for 10 mm shift case. Shift of the detector center causes to vary the distance of the readouts to collision point and this leads a variation in solid angle of the readouts. Comparing new and old solid angles, it was seen that the variation is not significant in the case of 10 mm shift. Since variation in solid angle does not affect total energy deposition, it can be interpreted as that change of the total energy deposition is caused by variance

of the energy spectrum.

Variation of the energy deposition is analyzed for both Generator level and Reconstruction level. At Generator level, total energy of the particles passing through the readouts is determined using positions of the readouts before and after shift. It is seen that uniformity of the total energy flow are spoiled due to the shift. High $i\eta$ rings are affected more compared to low $i\eta$'s as expected. In order to parametrize the behavior of the energy flow, Landau function is fitted to the energy density distribution as shown in Figure 4.14. Then, energy flow is calculated by using the fit function. In order to analyze goodness of the model, χ^2 values are calculated for the shift values from 0 mm to 20 mm. Minima of χ^2 is located at 10 mm and value is very close to zero. This shows that the model perfectly fits the data. We can conclude that reason of the variation in the energy deposition at generator level is the shift of energy spectrum.

Processes stated above are also applied at the Reconstruction level. Deposited energy calculated from the fit function work very well for low $i\eta$ rings. However, they do not fit well for high $i\eta$ rings. As it is seen in the distributions in Figure 4.22 and 4.24, sinusoidal shapes of energy flow for high $i\eta$ rings are degenerated and invariance of the total energy per ring ruined. According to geometrical model used, the shape should be sinusoidal and total energy per readout should not change due to shift. Therefore, variation in the energy flow at Reconstruction does not only depend on geometrical effects.

In order to identify other effects, different shift values in other direction need to be studied. Moreover, instead of min-bias events, particles making electromagnetic shower such as photon and electron could be chosen due to small shower length. After the other effects are understood, they could be integrated into the model and variation in the energy deposition can be explained in a better way.

REFERENCES

[1] D. Griffiths. *Introduction to Elementary Particles.* WILEY-VCH, 2nd edition, 2008.

[2] D. H. Perkins. *Introduction to High Energy Physics.* Cambridge University Press, 4th edition, 2000.

[3] C. G. Tully. *Elementary Particle Physics in a Nutshell.* Princeton University Press, 1st edition, 2011.

[4] B. R. Martin. *Nuclear and Particle Physics.* WILEY, 1st edition, 2006.

[5] R. Mann. *An Introduction to Particle Physics and the Standard Model.* CRC press, 1st edition, 2010.

[6] W. R. Leo. *Techniques for Nuclear and Particle Physics Experiments.* Springer-Verlag, 2nd edition, 1994.

[7] A. Penzo and Y. Onel. *The CMS-HF Quartz Fiber Calorimeters.* AIP Conference Proceedings of XIII International Conference on Colorimetry in High Energy Physics, 2009.

[8] M. Thomson. *Modern Particle Physics.* Cambridge University Press, 1st edition, 2013

[9] Particle Data Group. *Review of Particle Physics.* Elsevier, Volume 667, 2008.

[10] CMS Collaboration. *CMS Physics Technical Design Report Volume I: Detector Performance and Software.* CERN, Geneva, 2006.

[11] CMS Collaboration. *The CMS experiment at the CERN LHC.* JINST, 3(S08004), 2008.

[12] CMS Collaboration. *CMS Technical Design Report for the Phase 1 Upgrade of the Hadron Calorimeter.* CERN, Geneva, 2012.

[13] CMS Colobration. *Design, Performance and Calibration of the CMS Forward Calorimeter Wedges.* CMS-NOTE-2006-044, 2006.

[14] Olga Kodolova. *HCAL ϕ Symmetry Calibration.* Talk given at HCAL Workshop https://indico.cern.ch/event/367355/session/0/contribution/32/attachments/730337/1002101/phi_symmetry_050215.pdf

[15] Particle data group. http://pdg.lbl.gov/, Last accessed on 14/11/2015.

[16] HF Allignment. https://twiki.cern.ch/twiki/bin/viewauth/CMS/HFAlignment, Last accessed on 20/11/2015.

[17] Olga Kodolova. *HCAL calibration in high luminosity environment.* CMS Workshop: Perspectives on Physics and on CMS at Very High Luminosity, HL-LHC, Alushta, Crimea, Ukraine, 28-31 May 2012, p.169-175.

[18] Perrie Leon Cole. *Calibration Techniques for the Forward Hadron Calorimeter of the Compact Muon Solenoid.* MS thesis, UNIVERSITY OF MINNESOTA, 2010.

[19] Calorimeters. http://www.desy.de/ garutti/LECTURES/ParticleDetectorSS12 /L10_Calorimetry.pdf

[20] T. S. Virdee. *Physics requirements for the design of the ATLAS and CMS experiments at the Large Hadron Collider.* , Phil. Trans. R. Soc. A (2012) 370, 876–891.

[21] Cemali Kılınç. *The Effect of HF Shift on Phi Symmetry.* Talk given at HCAL Calibration Group, https://indico.cern.ch/event/389954/contribution/7/attachments/780054 /1069581/THE_EFFECT_OF_HF_SHIFT_ON_PHI_SYMMETRY4.pdf

[22] Cemali Kılınç. *The Effect of HF Shift on Phi Symmetry.* Talk given at HCAL Calibration Group, https://indico.cern.ch/event/344260/contribution/6/attachments/677542 /930916/THE_EFFECT_OF_HF_SHIFT_ON_PHI_SYMMETRY.pdf

[23] Anthony Richard Moeller. *Forward physics in CMS : simulation of PMT hits in HF and Higgs mass reconstruction methods with a focus on forward jet tagging.* PhD thesis,University of Iowa,2014.